Context Camera Investigation on board the Mars Reconnaissance Orbiter

Michael C. Malin,[1] James F. Bell III,[2] Bruce A. Cantor,[1] Michael A. Caplinger,[1] Wendy M. Calvin,[3] R. Todd Clancy,[4] Kenneth S. Edgett,[1] Lawrence Edwards,[5] Robert M. Haberle,[5] Philip B. James,[4] Steven W. Lee,[6] Michael A. Ravine,[1] Peter C. Thomas,[2] and Michael J. Wolff[4]

Received 9 August 2006; revised 15 November 2006; accepted 15 January 2007; published 18 May 2007.

[1] The Context Camera (CTX) on the Mars Reconnaissance Orbiter (MRO) is a Facility Instrument (i.e., government-furnished equipment operated by a science team not responsible for design and fabrication) designed, built, and operated by Malin Space Science Systems and the MRO Mars Color Imager team (MARCI). CTX will (1) provide context images for data acquired by other MRO instruments, (2) observe features of interest to NASA's Mars Exploration Program (e.g., candidate landing sites), and (3) conduct a scientific investigation, led by the MARCI team, of geologic, geomorphic, and meteorological processes on Mars. CTX consists of a digital electronics assembly; a 350 mm f/3.25 Schmidt-type telescope of catadioptric optical design with a 5.7° field of view, providing a ~30-km-wide swath from ~290 km altitude; and a 5000-element CCD with a band pass of 500–700 nm and 7 μm pixels, giving ~6 m/pixel spatial resolution from MRO's nearly circular, nearly polar mapping orbit. Raw data are transferred to the MRO spacecraft flight computer for processing (e.g., data compression) before transmission to Earth. The ground data system and operations are based on 9 years of Mars Global Surveyor Mars Orbiter Camera on-orbit experience. CTX has been allocated 12% of the total MRO data return, or about $\geq$3 terabits for the nominal mission. This data volume would cover ~9% of Mars at 6 m/pixel, but overlapping images (for stereo, mosaics, and observation of changes and meteorological events) will reduce this area. CTX acquired its first (instrument checkout) images of Mars on 24 March 2006.

Citation: Malin, M. C., et al. (2007), Context Camera Investigation on board the Mars Reconnaissance Orbiter, *J. Geophys. Res.*, *112*, E05S04, doi:10.1029/2006JE002808.

1. Introduction

[2] Imaging systems could be considered the most scientifically productive instruments of planetary exploration. Examples of scientific productivity from imaging systems include images that revealed active eruptions on Io, Triton (Voyager), and Enceladus (Cassini); showed the volcanoes, valley networks, and outflow channels of Mars (Mariner 9); documented an anthropogenic impact on a comet (Deep Impact); and permitted the first views of landscapes acquired from the surfaces of Venus (Venera) and Titan (Huygens). The Mars Reconnaissance Orbiter (MRO) Project, acknowledging the contribution of imaging systems to planetary exploration, carries four such systems: CRISM, the Compact Reconnaissance Imaging Spectrometer for Mars [*Murchie et al.*, 2007], HiRISE, the High Resolution Imaging Science Experiment [*McEwen et al.*, 2007], MARCI, the Mars Color Imager [*Malin et al.*, 2001a], and CTX, the Context Camera.

[3] The NASA MRO spacecraft, managed by the Jet Propulsion Laboratory (JPL), was launched aboard an Atlas V-401 from Launch Complex 41 at Cape Canaveral Air Force Station, Florida, on 12 August 2005, and entered orbit about Mars on 10 March 2006. Following a period of aerobraking to adjust the MRO orbit, the spacecraft will begin routine operations in the last quarter of 2006. On board the MRO, the Context Camera is designed to obtain 30-km-wide, $\geq$40-km-long, 5–6.5 m/pixel views of the Martian surface from the nominal 255–320 km altitude Primary Science Phase (PSP) orbit at ~15:00 local time. These images will provide spatial context for other MRO observations, and expand upon the results of previous high spatial resolution imaging investigations, particularly those of the Mars Global Surveyor (MGS) Mars Orbiter Camera (MOC). Because the MRO spacecraft can be rolled off

[1]Malin Space Science Systems, San Diego, California, USA.
[2]Department of Astronomy, Cornell University, Ithaca, New York, USA.
[3]Department of Geological Sciences, University of Nevada, Reno, Nevada, USA.
[4]Space Science Institute, Boulder, Colorado, USA.
[5]NASA Ames Research Center, Moffett Field, California, USA.
[6]Denver Museum of Nature and Science, Denver, Colorado, USA.

Copyright 2007 by the American Geophysical Union.
0148-0227/07/2006JE002808

nadir, such that its instruments can be pointed at specific targets on the Martian surface, CTX will be able to acquire stereoscopic image pairs and images that mosaic together to map areas $\geq$60 km wide from east to west.

[4] CTX was not selected by competitive proposal; rather, it was an outgrowth of the originally proposed Mars Climate Orbiter (MCO) MARCI Medium Angle camera [*Malin et al.*, 2001a] and recommendations of the MRO Science Definition Team empanelled by NASA. The MARCI development team was tasked by NASA with developing a new camera to serve three scientific purposes: (1) provide context for data acquired by other MRO instruments, (2) investigate features of interest to the NASA Mars Exploration Program, and (3) conduct investigations of ancient and contemporary geologic, geomorphic, and meteorological (dust raising events) processes on Mars.

[5] As a NASA Facility Instrument (an instrument selected as government-furnished equipment (GFE) to be operated by a science team not responsible for its design and fabrication), designed, developed and operated by Malin Space Science Systems (MSSS), CTX will provide context images for the MRO HiRISE [*McEwen et al.*, 2007], targeted observations CRISM context imaging [*Murchie et al.*, 2007], surface context observations for SHARAD (the Shallow Radar subsurface sounding system), and comprehensive views of candidate sites being considered by NASA for future Mars landings, including Phoenix (2007 launch) and the Mars Science Laboratory (2009 launch).

2. Science Objectives and Goals

[6] More than eight years of experience imaging the Martian surface at high spatial resolution by the MGS MOC experiment has shown new, and in some cases unexpected, details about the most recent, and the most ancient, events and processes that shaped the planet's surface and geologic record [*Malin and Edgett*, 2001, 2005]. Early in the mapping phase of the MGS mission, it became clear to the science team that MOC's high-resolution capability had crossed a threshold beyond which landforms and details observed at spatial resolutions better than $\sim$6–7 m/pixel provided a view of Mars very different than that offered by the highest-resolution Viking orbiter images (typically 8–30 m/pixel). Many of the results of the MOC investigation, now familiar to most geologists studying Mars, were a direct product of the higher spatial resolution. MOC images of resolution poorer than $\sim$6–7 m/pixel generally resembled the higher-resolution Viking images, or the Mars Odyssey Thermal Emission Imaging System (THEMIS) visible subsystem (VIS) images ($\sim$18 m/pixel). MRO CTX images will be similar to the high-resolution views from MOC, particularly in the sense that they are being acquired at a spatial scale that is better than the $\sim$6–7 m/pixel threshold. Many MOC images were acquired at $\leq$6 m/pixel (by spatially aggregating pixels), especially in locations such as west Candor Chasma and northern Sinus Meridiani, where there are vast exposures of layered rock, in order to maximize spatial coverage without sacrificing key details of the planet's geomorphology and stratigraphy.

[7] As a scientific investigation of the MRO MARCI/CTX team, CTX will be used to examine an array of topics that emerge directly from the results of the Mars missions conducted over the past decade. These objectives are to document and study the geology and geomorphology of (1) layered rock outcrops, their geologic records, and their denudation; (2) fluvial landforms and processes, including gullies, valley networks, and outflow channels; (3) eolian landforms, processes, and events; (4) mass movement processes; (5) polar landforms and processes; (6) volcanic features; (7) middle-latitude landforms; and (8) impact craters.

2.1. Layered Rock Outcrops

[8] On Earth, layers provide the books and pages from which the planet's geologic history is read. Layers are ubiquitous in the upper crust of Mars; they are exposed in crater and trough walls throughout the Martian highlands, they are found on the northern plains, and they comprise the walls of volcanic calderae [*Malin and Edgett*, 2001]. Layered materials on Mars are directly related to the relative roles of processes (water and wind erosion and deposition, volcanism, and impact cratering) that have acted upon the planet's surface at one time or another. Owing to the complex interbedding of layered rock, impact craters, and ancient valleys, the upper crust of Mars should be thought of as a volume, with landforms originally once at the surface (e.g., craters, valley networks, etc.) now distributed in three-dimensions throughout that layered volume [*Malin*, 1976; *Edgett and Malin*, 2004].

2.1.1. Light-Toned, Layered Rock Outcrops

[9] Of particular interest to the CTX investigation is the array of light-toned, layered exposures described by *Malin and Edgett* [2000a] as likely outcrops of sedimentary rocks. These outcrop areas are among the most important findings of the MGS MOC investigation. Observations of an eroded, fossil delta with inverted fluvial channels by MOC, plus the light-toned, layered bedrock of Meridiani Planum examined by the Mars Exploration Rover, Opportunity (MER-B), have confirmed that at least some of these materials are indeed sedimentary rocks [*Malin and Edgett*, 2003; *Squyres and Knoll*, 2005]. Primary igneous materials (i.e., tephra deposits) have also been proposed to occur in some locations and in forms that might be challenging to distinguish from sedimentary materials in orbiter images [*Scott and Tanaka*, 1982; *Chapman*, 2002]. Highly repetitious beds or packages of bedded material, like those in southwest Candor Chasma [*Malin and Edgett*, 2000a] or in some of the craters of western Arabia Terra (Figure 1), suggest that cyclic or at least episodic change occurred in some environmentally modulated depositional settings. Vertical changes in bedding properties, such as slope morphology (a function of resistance to erosion), reflect temporal changes in the caliber or composition of material deposited and/or the diagenesis of the materials. Unconformities, particularly erosional unconformities, have also been observed in some outcrop areas, such as Gale Crater and northern Sinus Meridiani [*Malin and Edgett*, 2000a; *Edgett*, 2005]. The light-toned outcrops, in addition to their morphologic characteristics, also in some cases present key near infrared spectroscopic evidence for sulfate and phyllosilicate mineralogies [*Gendrin et al.*, 2005; *Arvidson et al.*, 2005; *Poulet et al.*, 2005].

[10] CTX images will provide context for and fill gaps in coverage between 1.5–6 m/pixel MOC narrow-angle

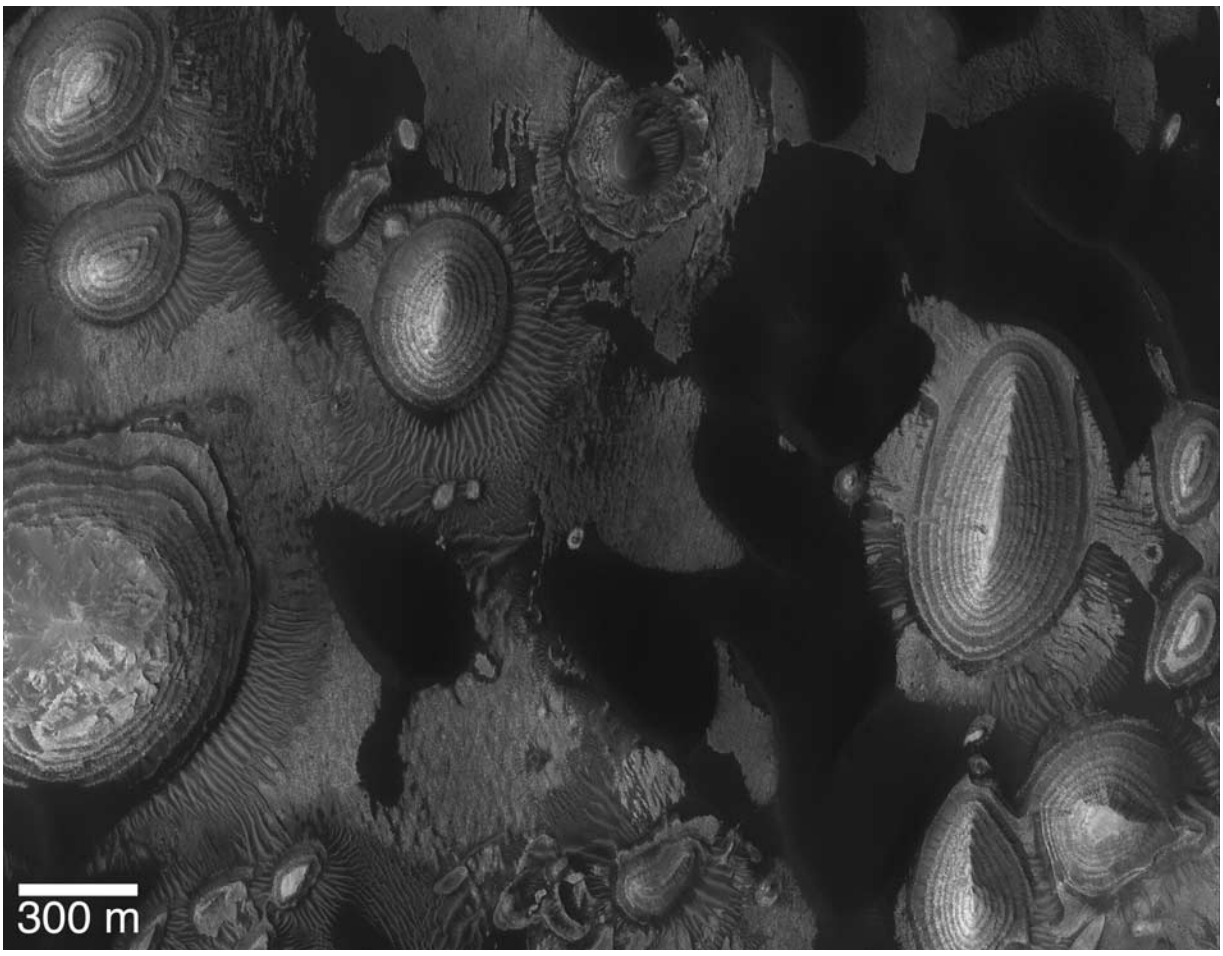

Figure 1. Eroded remnants of rhythmically bedded, light-toned, sedimentary rock in a crater in western Arabia Terra at 8.9°N, 1.2°W. This is a subframe of MOC image S07-00608; north is toward the top/upper right. The sun shines from the left.

camera images and the new MRO HiRISE data of light-toned layered rock. Stereopairs of CTX images, particularly when acquired during what is known for each outcrop location to be the best time of year for high-resolution imaging in terms of low atmospheric opacity and higher solar incidence angle, will help investigators trace stratigraphic relations over greater distances than can be easily accomplished with existing MOC coverage. CTX will also be employed to look for previously undocumented outcrop sites. MOC images show that there are scattered, small (<1 km across), light-toned, layered rock outcrops on the upland plains through which the central troughs of the Valles Marineris are cut and in the heavily cratered terrain south of Meridiani Planum [*Edgett*, 2005]. CTX, with its 30-km-wide field of view, will facilitate locating additional outcrops in these regions much more quickly than possible with MOC 3-km-wide swaths. CTX will also be employed to document and help piece together the stratigraphic, deformational, and structural attributes of the layered materials in northwest and southeast Hellas Planitia and central Argyre Planitia, particularly during the mid-late southern autumn season ($L_s \sim 55°-85°$), when atmospheric opacity is low and solar incidence angles are ideal (e.g., Figure 2).

2.1.2. Denudation of Light-Toned, Layered Rock Outcrops

[11] One of the most important mysteries to emerge from the MGS MOC investigation is the extreme paucity of impact craters on the surfaces of exposed, light-toned, layered rock outcrops [*Malin and Edgett*, 2001]. The problem is best illustrated in western Candor Chasma, where the upland surrounding the chasm and the walls of the chasm exhibit hundreds of subkilometer diameter impact craters, but the interior light- and intermediate-toned layered rocks do not. *Hartmann* [2005] used crater counts to estimate the age of the floor of the caldera of Arsia Mons to be 200–1000 million years. In other words, the caldera floor of Arsia Mons is generally considered to be geologically young. Figure 3 compares equally sized areas (representative of surfaces of 1000s km^2 extent), one on the floor of the Arsia Mons caldera, the other shows layered rock outcrops in west Candor Chasma. The Arsia Mons surface is peppered with small impact craters, the other has none. If the abundant small craters in the caldera of Arsia Mons imply a relatively young age, does the absence of craters in west Candor imply that the processes of denudation and exposure of these outcrops has occurred extremely recently,

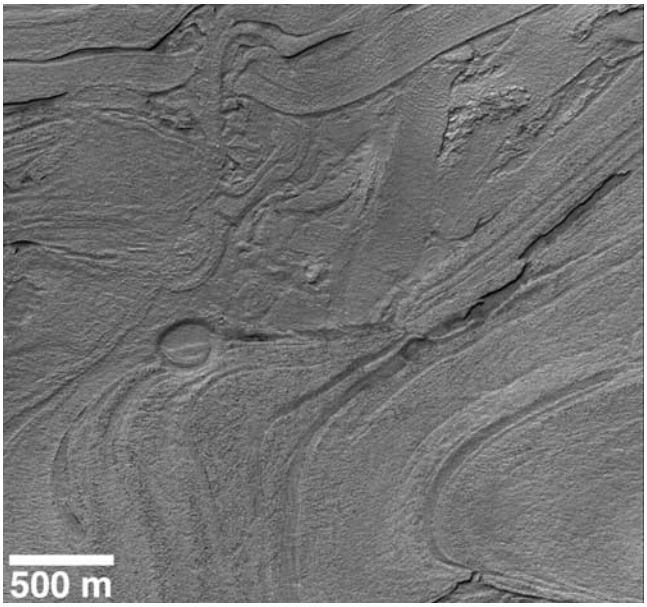

Figure 2. Complexly exposed and deformed(?) layered rock in northwestern Hellas Planitia. This is a subframe of MOC image S14-02611, located near 40.7°N, 307.5°W. The image covers an area 3 km across; north is toward the top/upper right. The illumination is from the upper left.

and is active in the present Martian environment? The materials are not covered with dust or sand; how are they being eroded and where did (or are) the products of this erosion going? Elsewhere on Mars, some light-toned rock outcrop sites exhibit wind-eroded yardangs, for example in Trouvelot Crater [*Malin and Edgett*, 2001], but many of these outcrops show little evidence regarding how they came to be eroded and exposed at the present Martian surface.

[12] A key activity of the CTX science investigation will be to acquire a full mosaic (and stereopair coverage) of western Candor Chasma, permitting a more complete documentation of its impact crater population than has been possible with the previous acquisition of dozens of MOC narrow-angle images. The majority of MOC images of west Candor were, in fact, obtained at better than 6 m/pixel scale. If evident, eolian sediment transport pathways in Candor and other chasms in which similar rock outcrops occur will be documented to further understand the denudation processes that have acted on these materials. Imaging relatively large areas (100s to 1000s km^2), such as all of west Candor or the layered mound of rock in Gale Crater, will ensure that all impact craters on these surfaces, down to about 20 m diameter, will be documented. Erosional landforms, such as the yardangs common on the light-toned outcrops of west Tithonium Chasma, or the fine-scale fluvial forms preserved in rock in southwestern Melas Chasma, will also be examined.

2.2. Fluvial Features

[13] Fluvial features, or at least features for which investigators have proposed fluvial origins, include the relatively large outflow channels, relatively small middle- and polar-latitude gullies, and the intermediate-scale valley networks. CTX observations will enhance studies of these Martian features, commonly considered to be the products of erosion by liquid water.

2.2.1. Gullies

[14] *Malin and Edgett* [2000b] first described middle- and high-latitude gullies. Nearly all examples occur poleward of 30° latitude in both hemispheres. Gullies found equatorward of 30° are very rare; the majority of these are poleward of 27° and most of these occur on the north walls of Nirgal

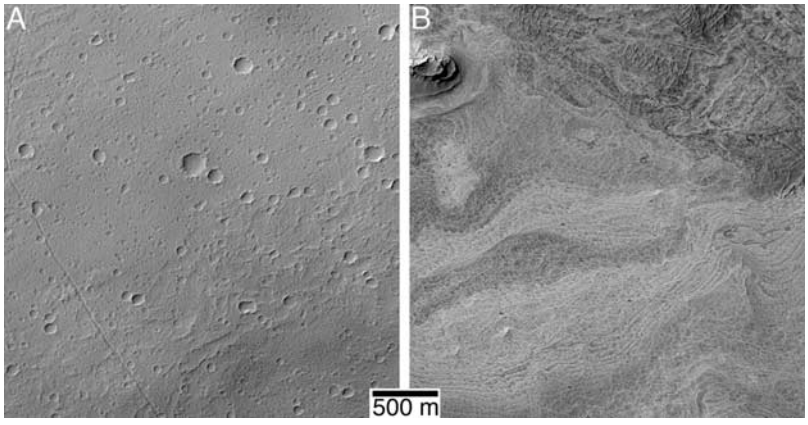

Figure 3. Comparison of small crater populations on the floor of (a) the Arsia Mons caldera and (b) western Candor Chasma. Although the caldera floor is considered to be quite young on a geologic timescale, the surface in west Candor must be even younger, so young that perhaps processes that remove craters from this surface still occur today. Both images were taken about the same time of year under similar illumination conditions (sunlight from the left/upper left). Both were acquired at 6 m/pixel, the scale of CTX images. (a) Subframe of MOC image E03-00354, near 9.0°S, 120.7°W. (b) Subframe of MOC image M02-00343, near 6.1°S, 75.7°W. North is toward the top/upper right in both images. Illumination is from the upper left.

Vallis. Gullies always have a channel and typically exhibit an apron, unless it has been buried. Channels are commonly banked and sinuous, but in some cases they meander. Examples of straight channels also exist. The channels usually originate at a point about 200–800 m below the local surface outside of the depression in which the gully occurs [*Malin and Edgett*, 2000b; *Gilmore and Phillips*, 2002; *Heldmann and Mellon*, 2004]. In some cases, the aprons include dozens to hundreds of individual flow lobes. Many, although not all gullies have an alcove above the channel; these form by undermining, collapse, and mass movement of debris [*Malin and Edgett*, 2000b]. The majority of the tens of thousands of gullies occur in the walls of craters, pits, valleys, troughs, and depressions. However, some variants occur on dune slip faces, crater central peaks, and the mountains around Argyre Planitia [*Malin and Edgett*, 2000b; *Baker*, 2001; *Reiss and Jaumann*, 2003], although differences in specific morphology may reflect alternative origins.

[15] A few hypotheses for the origin of the gullies center on release of subsurface CO_2 [*Musselwhite et al.*, 2001; *Hoffman*, 2002]; *Stewart and Nimmo* [2002] considered it unlikely that sufficient quantities of CO_2 could be trapped beneath the surface. Other investigators suggested that the gullies formed by dry, granular flow, without the participation of water or CO_2 [*Treiman*, 2003; *Shinbrot et al.*, 2004]. However, banking, contributory channeling, meanders and meandering sinuosity, and flow lobes in apron deposits are clues that the rheologic properties of the flows that came through at least some gullies required the presence of a fluid with the rheological properties of liquid water [*Malin and Edgett*, 2000b; *Hartmann et al.*, 2003]. Among hypotheses that favor liquid water are those centered on groundwater [*Malin and Edgett*, 2000b; *Mellon and Phillips*, 2001; *Gilmore and Phillips*, 2002; *Heldmann and Mellon*, 2004], melting ground ice [*Costard et al.*, 2001], and melting surface ice or snowpack [*Lee et al.*, 2001; *Christensen*, 2003]. The gullies occur over a wide range of settings, most of them very far from volcanic regions, suggesting that volcanic and hydrothermal processes are not involved [*Malin and Edgett*, 2000b]. The groundwater hypothesis may be favored by key 2005–2006 MOC observations that demonstrate correlations between some gullies with overhanging layers, faults, and small impact craters (Figure 4).

[16] The majority of the tens of thousands of gullies identified in MOC and THEMIS images are not cratered. The few that are cratered typically have multiple, closely spaced small craters, suggesting that these are cases of secondary impact [*Edgett et al.*, 2003a]. Estimates of the age of gullies center on their geomorphic and stratigraphic youth and lack of superposed impact craters. *Malin and Edgett* [2000b] concluded that the gullies could be less than 1 million years old. *Reiss et al.* [2004] examined small craters on eolian megaripples in Nirgal Vallis, which are also superposed by gully aprons, and concluded that these may be

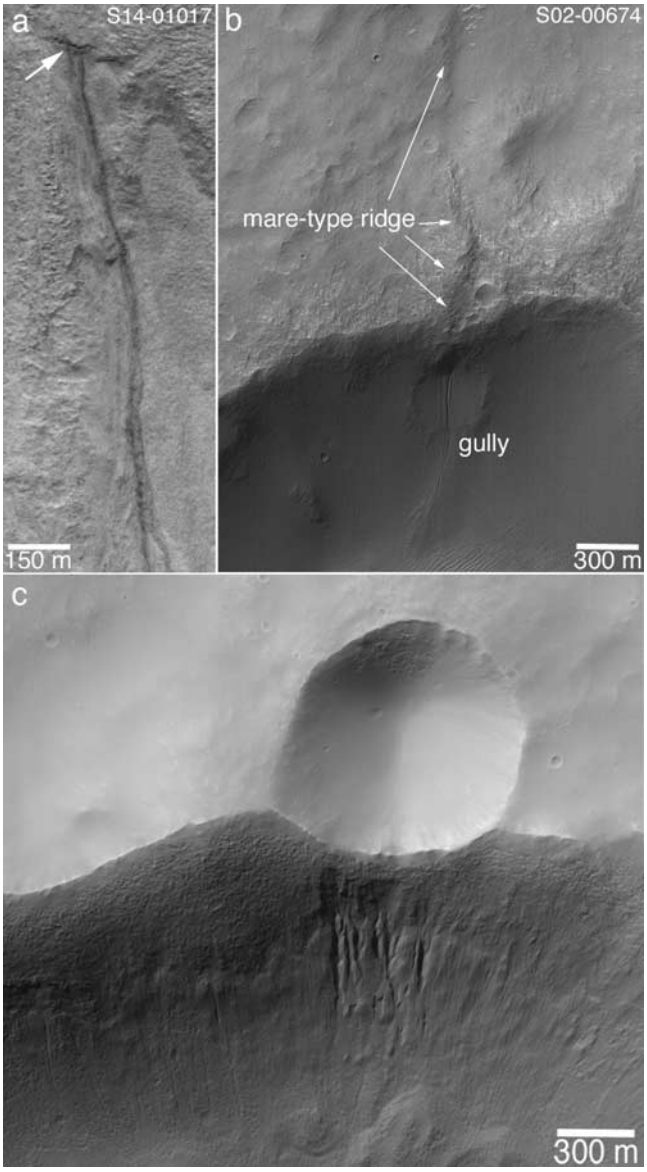

Figure 4. Evidence for groundwater role in midlatitude gully genesis. (a) A gully channel heads just below an overhanging rock layer in the wall of Dao Vallis. Gullies on the walls of Dao Vallis are considered by others [e.g., *Christensen*, 2003] to have attributes that serve as prime examples of a key alternative explanation, snowmelt. This example is from a subframe of MOC image S14-01017, located near 34.2°S, 268.1°W. (b) A gully head associated with intersection of a mare-like ridge and the crater wall, at a fault. The gully is also located equatorward of 30°S and provides key evidence for involvement of groundwater in gully genesis because water would have taken advantage of the presence of a fault such that it emerges where the fault and surface environments intersect. The picture, a subframe of MOC image S02-00674, is located near 29.1°S, 207.5°W. (c) Gullies located on a crater wall, below the site of a smaller impact crater. In this case the smaller impact postdates the larger crater in which the gullies occur. The additional fractures in the bedrock created by this smaller crater may have increased the availability of conduits through which groundwater could come to the surface and create the gullies. This is a subframe of MOC image S16-02714, located near 33.9°S, 160.0°W. In all three images, north is toward the top/upper right. The sun shines from the left/upper left.

younger than 3 million years, and perhaps < 300,000 years. Other investigators have focused on the role of obliquity excursions to promote gully formation, and whether gullies might be active under temperature and pressure conditions different from those that occur today [*Costard et al.*, 2001; *Christensen*, 2003; *Berman et al.*, 2005]; however, the work of *Heldmann et al.* [2005] suggested that modern pressure and temperature conditions are a better fit when the measured run-out distances of gully channel/apron complexes are considered.

[17] CTX offers a key advantage over previous imaging systems at Mars. Its order of magnitude wider field of view, relative to MGS MOC, means that more gullies can be observed at a given locale within a single image acquired at a single time. In most depressions (especially impact craters) where gullies occur, MOC coverage is incomplete because multiple 3-km-wide images are required to map out the full suite of gullies at the given location, where only one or two CTX images are necessary. The other key advantage over previous systems, particularly the Mars Express High Resolution Stereo Camera (HRSC; best resolution ~10 m/pixel, but typically lower) and Mars Odyssey THEMIS VIS (~18 m/pixel), is spatial resolution. Most gullies are too small to be adequately identified and monitored for change in 18 m/pixel images, and even 10 m/pixel images do not show all of the relevant morphologic details. However, new gully locations have been routinely identified by targeting MOC images at 4.5–6.5 m/pixel, and CTX data fall within this range. With CTX, it will be possible to identify and monitor a larger number of gully sites than can be accomplished with MOC. *Malin and Edgett* [2000b] speculated that some gullies might be so young that new flow and depositional events might occur today, and the *Heldmann et al.* [2005] study supports this possibility. In this context, CTX will be employed to routinely re-image known gully locations to look for changes. CTX 6 m/pixel stereo views will enhance geomorphic studies and models that are focused on the nature of the slopes upon which gully channels occur.

2.2.2. Valley Networks

[18] Valley networks are often cited as key evidence that past Martian environments were considerably different from those of the present [e.g., *Milton*, 1973; *Sharp and Malin*, 1975; *Pieri*, 1976, 1980; *Mars Channel Working Group*, 1983], although some cases have also been described as perhaps being related to impact- or volcanic-induced conditions [e.g., *Maxwell et al.*, 1973; *Brakenridge et al.*, 1985]. Valley networks commonly display arborescent patterns, sinuous channels, and occasional meanders that imply processes of overland flow, drainage basin development, and sustained surficial transport of fluid. The origins of these valleys have remained controversial for the past three decades, with surface runoff fed by precipitation versus sapping fed by groundwater (perhaps requiring precipitation for recharge) being the main alternatives cited [*Sharp and Malin*, 1975; *Pieri*, 1980; *Malin and Carr*, 1999; *Grant*, 2000; *Craddock and Howard*, 2002; *Aharonson et al.*, 2002]. At orbiter image scales (~1.5–12 m/pixel range), the majority of valley networks appear to have been subjected to considerable modification since they formed. Their floors are commonly obscured by eolian megaripples, their walls have retreated as a result of mass wasting, and at middle latitudes materials have mantled and covered portions of key valley systems, such as those on Alba Patera and the Warrego Valles [*Malin and Carr*, 1999; *Carr and Malin*, 2000; *Malin and Edgett*, 2001; *Ansan and Mangold*, 2006].

[19] Analysis of MOC and THEMIS VIS images have also led to the recognition that portions of valley network systems are in some cases buried, or the rock into which the valleys cut has been removed by erosion, and some channels have been inverted by erosional processes. In other words, the valley network story for Mars is not entirely recorded on the planet's surface; it is also preserved in (or in some cases removed by erosion from) its rock record [*Williams and Edgett*, 2005]. Inverted channels are also common on eroded sedimentary fans, such as the fossil delta in Eberswalde Crater [*Malin and Edgett*, 2003] and the fans of Aeolis [*Williams and Edgett*, 2005]. Some networks that appear to be clearly resolved in 100 m/pixel scale thermal infrared images, such as those near Echus Chasma described by *Mangold et al.* [2004], are actually poorly integrated and severely eroded when observed at the scale of MGS MOC or MRO CTX images. Finally, some networks are of extremely fine scale, like that of terrestrial rills and creeks, and have been exposed from within the rock record by erosion and, in some cases, inversion; examples occur near Juventae Chasma [*Williams et al.*, 2005] and in southwestern Melas Chasma, where *Quantin et al.* [2005] have erroneously mapped a suite of integrated networks where high-resolution MOC images show only discontinuous channels and depositional fans located at different levels within a layered rock stratigraphy.

[20] CTX images will provide 6 m/pixel stereo and mosaic views of key valley network sites, including the features in southwestern Melas Chasma, on the plains immediately west of Juventae Chasma, Warrego Valles, Paraná Valles, northwestern Alba Patera, Auqakuh Vallis, and the fans in Aeolis. These detailed images will fill in critical gaps in the existing high spatial resolution coverage from MGS MOC and other orbiter imaging systems. Owing to its larger field of view, CTX will also contribute to mapping of valleys with known interior channels, often cited as evidence for sustained of fluvial activity [*Malin and Carr*, 1999; *Irwin et al.*, 2005; *Jaumann et al.*, 2005], despite the observation that the first such case identified, in Nanedi Valles, turned out to be a discontinuous feature [*Malin and Edgett*, 2001].

2.2.3. Outflow Channels

[21] The large Martian outflow channels, particularly the circum-Chryse valleys, have received considerable attention and discussion since they were first seen in Mariner 9 images. The presence of imbricated boulders at the Mars Pathfinder landing site [*Smith et al.*, 1997] generally confirmed the view that outflow channels seem to be the products of catastrophic flooding [*Baker and Milton*, 1974; *Sharp and Malin*, 1975; *Baker and Kochel*, 1979; *Carr*, 1979]. A major objective of the MGS MOC investigation was to use high spatial resolution images to examine the size and spatial distribution of debris (particularly large boulders) in outflow channel systems to help distinguish between models for outflow channel formation by catastrophic flood, debris flow activity, or action of glacial ice [*Malin et al.*, 1992]. However, very few boulders were resolved in these channels in MOC images of spatial

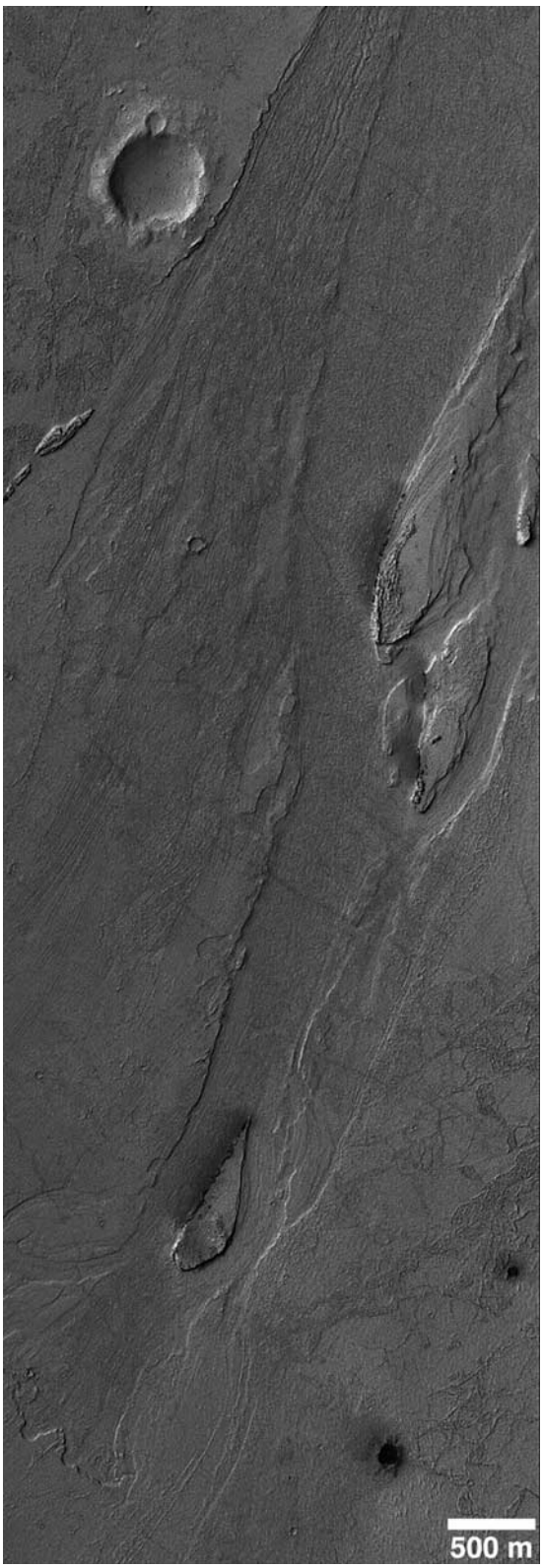

Figure 5. This is a portion of an unnamed outflow channel in the Zephyria region (south of Cerberus) of Mars. The image was acquired at 6 m/pixel, like CTX images, but covers an area only 3 km wide. Note the cataract at the lower left. Fluid flowed from the lower left toward the upper right. This is a subframe of MOC image R20-00043, located near 3.7°N, 204.7°W. Illumination is from the left.

resolution as high as 0.5–2.0 m/pixel [*Malin and Edgett*, 2001]; the boulders that are observed in the MOC images are commonly those found in the ejecta of impact craters that formed after the channels were cut. The Mars Pathfinder and Viking 1 lander sites show that large boulders do exist in some outflow channel settings, but those transported by the floods may generally be smaller than can be resolved in MOC, and hence CTX, images. We note that this is a promising area for MRO HiRISE observations.

[22] Images from MOC, THEMIS, and the Mars Express High Resolution Stereo Camera (HRSC), highlight attributes of the Kasei Valles, Marte Valles, and Athabasca Valles regions. Within Kasei Valles, MOC images show evidence for a relatively late-stage fluvial event or events, in which material flowed through the southernmost valley of the east Kasei Valles complex. This younger event in Kasei created a cataract through which water and mud appears to have flowed [*Williams and Malin*, 2004]. Images from MOC and THEMIS provided fresh, generally unanticipated details about features that may be among the youngest outflow channel features on Mars, including Marte Valles, Athabasca Valles, and other channels in the classical albedo regions of Cerberus and Zephyria (Figure 5). Much of the work on these features has focused on the confusing mix of evidence for catastrophic flood by water, flow of extremely fluid lavas, and perhaps mudflows, in the region [*Burr et al.*, 2002a, 2002b, 2004; *Berman and Hartmann*, 2002; *Head et al.*, 2003a; *Plescia*, 2003]. Other, smaller channel systems that bear some similarity to those in the Cerberus region occur in Tharsis, particularly in the regions east of Olympus Mons [*Mouginis-Mark*, 1990; *Mouginis-Mark and Christensen*, 2005].

[23] Owing to the larger field of view and MOC-scale spatial resolution, CTX is an excellent tool for furthering understanding of the outflow channel features observed in MOC and THEMIS images in the Kasei, Athabasca, Marte, and Tharsis regions. Lava flows draped over the west walls of western Kasei Valles and flowed for some distance into the valley. Valley floor geomorphology observable in the 30-km-wide CTX images will permit the opportunity to help distinguish these flows and their relationship to other features interpreted as possible mudflows [*Malin and Edgett*, 2001; *Williams and Malin*, 2004] in the Kasei Valles system. CTX will also be employed to build up 6 m/pixel mosaics and stereo views of key locations in the Marte, Athabasca, and similar valley systems in the Cerberus, Zephyria, Amazonis, and Tharsis regions.

2.3. Eolian Activity and Processes

[24] Eolian landforms and processes occur at the interface between a planet's atmosphere and surface. As such, eolian landforms record aspects of diurnal, seasonal, annual, and multiyear climate events. Eolian processes under Martian conditions transport fine-grained materials (dust, silt, sand, and granules) [*Iversen and White*, 1982]. Past climates may have had different wind regimes that transported different sizes or amounts of material. The same may be true of eolian erosion: large portions of the Martian surface have been deflated, producing yardangs of various orientations that do not match current wind patterns [*Ward et al.*, 1985; *Greeley et al.*, 1993]; and some show evidence that yardangs formed, then were buried by later yardang-forming

material, preserving a complex record of previous wind regimes [*Wells and Zimbelman*, 1989]. CTX will be used to acquire images that address aspects of contemporary and earlier eolian activity, including documentation of dust storms and dust devils, wind streaks, and eolian bedforms (dunes and megaripples).

2.3.1. Contemporary Activity

[25] Mars Global Surveyor MOC experience has demonstrated, over a period spanning more than 4 Mars years, that dust is raised somewhere on Mars nearly every day [*Cantor et al.*, 2001; *Cantor*, 2003]. Dust-raising events include dust devils, small plumes created by gusting winds, and dust storms of a variety of sizes ranging from local to regional in scale. *Cantor et al.* [2002] noted, after just a little more than one Mars years of MOC daily global observations, that some weather phenomena repeat year after year. For example, there is a dust storm that occurs every Mars year around L_s 139° south of and adjacent to Melas Chasma that was first observed by MOC in Mars approach images acquired during the MGS cruise phase on 2 July 1997. It was seen again in 1999, 2001, 2003, and 2005 at about the same time of year. These repeated events are believed to attest to a delicate energy balance within the Martian atmosphere, and the prevalence of threshold conditions in stimulating meteorological responses, relative to Earth. The predictability was sufficient to know more than a year in advance that a dust storm would occur in Isidis Planitia near the time of the Beagle 2 landing, and, indeed, this is what occurred on 11 December 2005, about 13 days before the landing attempt. CTX observations of dust-raising events and changes in wind streaks and albedo patterns over time will complement simultaneous observations obtained at different scales by the other MRO instruments, particularly the MARCI daily global images.

[26] Dust devils on Mars occur in a variety of sizes: some tower several kilometers and are readily seen from orbit, even in images of ~250 m/pixel, others contain so little dust that they are not readily seen from orbit, but are visible to landed instruments such as the cameras on the MER Spirit rover [*Cantor et al.*, 2006; *Greeley et al.*, 2006]. Some dust devils create streaks as they disrupt dust on the surface; both streaks and dust devils have been observed by Viking, MOC, THEMIS, and HRSC at nearly all latitudes and at elevations from the tops of the Tharsis volcanoes to the deepest parts of Hellas basin [*Thomas and Gierasch*, 1985; *D. A. Williams et al.*, 2004; *Cushing et al.*, 2005; *Cantor et al.*, 2006]. Except in the polar regions, dust devils are probably most abundant in the afternoon, peaking in the local time range between 11:00 and 15:00, much like their terrestrial cousins [*Sinclair*, 1969; *Ferri et al.*, 2003]. Four Mars years of MOC observations have shown that large, abundant dust devils are most common in three specific regions: northern Amazonis, a light-toned surface at the Syria Planum/Claritas Fossae boundary, and a light-toned surface in eastern Sinus Meridiani, west of Schiaparelli basin [*Cantor et al.*, 2006]. In the case of northern Amazonis, dust devils begin to be observed in the afternoon within two weeks of the start of northern spring, and then they occur nearly every day through spring, summer, and often into the first week or two of autumn; then they shut down for the rest of autumn and winter, when local dust storms are often observed instead of dust devils. MOC narrow-angle images of spatial resolutions in the 6–12 m/pixel range were routinely acquired in these known regions of dust devil activity, and they often captured multiple vortices despite having only a 3-km-wide field of view. CTX will be directed to monitor these three regions of known, frequent dust devil activity. If both MGS MOC and CTX are operating at the same time during the MRO Primary Science Phase, it may be possible to see whether any dust devils continue to be active over the 1-hour interval between the passage of MOC and CTX over these regions.

[27] Dust storms, as with dust devils, come in a variety of sizes and commonly occur at predictable times and pass through the same regions year after year [*Cantor et al.*, 2001; *Cantor*, 2003, 2007]. The occurrence of dust storms on Mars has been recognized for well over a century [*Martin and Zurek*, 1993] and can include planet-encircling events [*Zurek and Martin*, 1993; *Cantor*, 2007]. The most common dust storm activity is the product of cold winds blowing off the edge of the seasonal polar cap, in both hemispheres, particularly in their respective spring seasons. Owing to the predictability of some polar storms, it will be possible to target CTX images with the specific intent of catching some of these dust storms in action, at 6 m/pixel spatial resolution. MOC narrow-angle camera experience demonstrates that images such as these will help pinpoint dust sources, as opposed to the dust clouds that drift downwind from the source, by showing the streamers and gusts that are caught in the act of directly lifting dust from the Martian surface (Figure 6). Such data will compliment daily global observations from the MRO MARCI and MGS MOC in helping to understand where present sources for loose, unconsolidated dust are located.

[28] Contemporary eolian activity also includes the "variable features" of Mars. Changes in albedo pattern have been noted for over a century. With the advent of flyby and orbiter observations in the 1960s and 1970s, a suite of studies were conducted which examined the changing of albedo patterns and wind streaks as a function of season and in connection with the passing of dust storms through a given region [e.g., *Sagan et al.*, 1972, 1973; *Veverka et al.*, 1977; *Thomas and Veverka*, 1979; *Lee et al.*, 1982; *Greeley et al.*, 2005; *Geissler*, 2005]. Once attributed to vegetation [e.g., *Lowell*, 1896], it became clear that these changes are caused by wind redistribution of relatively thin veneers of dust [e.g., *Sagan and Pollack*, 1969; *Greeley et al.*, 1974; *Christensen*, 1988]. Throughout the 1 Mars year Primary Science Phase of the MRO mission, CTX images of key locations where wind streaks, dust devil tracks, and other variable albedo features are known to occur will be imaged to compare with or complement other data acquired of these same targets over the previous few decades. Several sites where wind streak changes have been noted by ongoing MGS MOC monitoring will be examined, including repeated observations of the regions around the two Mars Exploration Rovers, both of which have exhibited changes in wind streak and albedo patterns during the past few Martian years [*Greeley et al.*, 2005; *Sullivan et al.*, 2005; *Cantor et al.*, 2006]. These phenomena are important as they provide key constraints on the availability and mobility of surface fines and on the conditions necessary for their movement.

Figure 6. Example of a Martian dust-raising event viewed at 6 m/pixel. The wind was blowing from the bottom toward the top of the frame, lifting dust from the ground in dozens of small streamers and creating a plume downwind. The image covers an area 3 km wide; sunlight illuminates the scene from the upper left. This is a subframe of MOC image E11-01671, located near 87.0°S, 170.4°W. Illumination is from the left.

[29] Contemporary albedo changes and the physical properties of surface materials can also be investigated with select CTX observations. CTX images of the opposition surge near zero phase can be used for photometric studies of surface properties [e.g., *Thorpe*, 1982]. Because of its relatively broad visible-wavelength band pass, CTX radiance data can be converted to an approximate (or scaled) bolometric albedo for monitoring of surface albedo features in comparison with previous orbital and telescopic albedo observations [e.g., *Pleskot and Miner*, 1981; *Christensen*, 1988; *Christensen et al.*, 2001]. Such data also are useful for cross-calibration with other MRO imaging and spectroscopic instruments, and for comparison with surface-based albedo measurements [e.g., *Bell et al.*, 2004].

2.3.2. Bedforms

[30] Eolian dunes are composed mainly of sediment transported by saltation; ripples typically consist of particles moved by the impact of saltating grains [*Sharp*, 1963]. Dunes and very large ripples (megaripples) are readily observed in orbiter images, especially the higher-resolution views [*Cutts and Smith*, 1973; *Tsoar et al.*, 1979; *Thomas et al.*, 1999; *Wilson and Zimbelman*, 2004; *Yizhaq*, 2005]. Comparisons between dune positions in Mariner 9 and Viking orbiter images with MGS MOC images (and MOC images with earlier MOC images) of dunes and large ripples have not yet revealed any evidence that the bedforms have moved during the past Martian decade [*Edgett and Malin*, 2000; *Zimbelman*, 2000; *Edgett*, 2002; *Schatz et al.*, 2006]. Terrestrial experience shows that small dunes move more quickly and will travel the greatest distance [*Finkel*, 1959; *Long and Sharp*, 1964]. One series of MOC images showed that a couple of small, dark patches of sand moved, but the larger, neighboring dunes did not (Figure 7).

[31] CTX will extend forward in time the efforts of the MGS MOC, underway since 1997, to re-image dunes and dune fields (particularly those areas with the smallest barchans) as well as large eolian ripples, to help determine, at least to 6 m/pixel scale, whether any of these bedforms are changing or have changed since previous images (Mariner 9, Viking, or MGS) were acquired. The advantage of CTX over the preceding MOC effort is its greater field of view, permitting more dunes at a given location to be examined in a single image, and the likelihood that CTX will be operating farther in the future than MOC. CTX will also be employed to extend the MOC effort to repeatedly monitor dunes subjected to the coming and going of seasonal frost, such as those in Richardson Crater [*Supulver et al.*, 2001]; to look for changes on dune slip faces, such as the formation of a new avalanche chute or gully in the Russell or Kaiser dune fields [*Reiss and Jaumann*, 2003]; and to document the nature of buried or exhuming dunes and sand-rich beds in the north polar region [*Edgett et al.*, 2003b; *Schatz et al.*, 2006].

2.4. Mass Movement

[32] Contemporary processes on Mars include mass movements, such as the formation of new streaks by downhill motion of material on dust-mantled slopes and the rolling of boulders to form new boulder tracks. MGS MOC has documented the products of both of these processes at spatial resolutions comparable to CTX, although the majority of boulder tracks are better seen at higher resolution. Boulder tracks are commonly created on Earth, the Moon, and Mars, when boulders roll down slopes of materials having physical properties that will preserve the depressions made by a bouncing and/or rolling object [e.g., *Eggleston et al.*, 1968].

[33] Slope streaks, which include some that are darker than and others that are lighter than their surrounding surfaces, are more common than boulder tracks. The majority occur in the dust-mantled regions of Tharsis, Arabia, Tempe Terra, and hillslopes adjacent to Amazonis Planitia and the plains south of Cerberus [*Sullivan et al.*, 2001; *Aharonson et al.*, 2003]. Some investigators have proposed that water may be involved in the formation of slope streaks [*Schorghofer et al.*, 2002; *Ferris et al.*, 2002], but others suggest, in large part on the basis of the fact that they only occur on dust-mantled surfaces, that they are

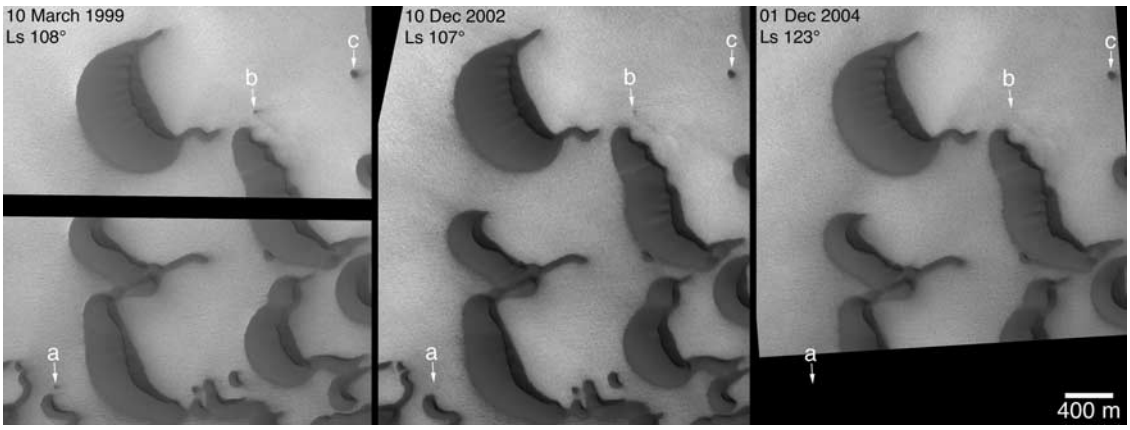

Figure 7. Evidence for contemporary transport of eolian sand on Mars. While the large north polar dunes have not moved during this sequence of images obtained during 1999–2004, two small patches, labeled a and b, changed. Patch a disappeared between March 1999 and December 2002, while patch b steadily got smaller. Patch c, which is larger than patches a and b, does not appear to have changed. The changes observed (as well as changes that should have occurred but did not) suggest that the larger dunes are crusted and only a very small amount of the local sand is loose and available for transport in the modern environment. Winds are strong enough to move sand in the north polar region, because summertime dust storms are common, and winds capable of moving dust are stronger (or the same if sand launches dust by saltation impact) than those needed to move sand. These images are located near 76.4°N, 264.9°W. Left: subframe of MOC image FHA-00515. Middle: MOC image E23-00490. Right: MOC image S01-00007. Illumination is from the lower left.

simply the product of dry avalanching of the dust [*Sullivan et al.*, 2001]. New slope streaks have been seen in MOC images to have formed over intervals as short as 100 days [*Sullivan et al.*, 2001; *Aharonson et al.*, 2003]. With its large field of view, relative to MOC, CTX will be used to re-image known locations of slope streaks previously observed by Viking, MOC, THEMIS VIS, and HRSC, to further document the rate and frequency of change.

[34] CTX images will also document and provide 6 m/pixel stereo views of landslide deposits on Mars. Those in the Valles Marineris [*Lucchitta*, 1978; *McEwen*, 1989], for example, are typically wider than the MOC 3 km field of view, and very few examples have been fully documented by building up mosaics of MOC images. High-resolution images of such landslides contribute to studies of the physical properties of the material during emplacement [*Malin and Edgett*, 2001], which aids in addressing the long-standing question of whether the very large landslides on Mars contained and released water and/or involved dry granular flow processes [*Soukhovitskaya and Manga*, 2006].

2.5. Polar Processes and Landforms

[35] During the past nine years, Mars Global Surveyor, Mars Odyssey, and Mars Express have provided a quantum leap in knowledge about the Martian polar regions. New features have been observed, including the dynamic, changing mesas and circular pits of the south polar residual cap [*Thomas et al.*, 2000; *Malin et al.*, 2001b], evidence for water ice, in addition to CO_2, in the south polar region [*Titus et al.*, 2003; *Bibring et al.*, 2003], dynamic and unexpected patterns on dunes and regolith surfaces in the defrosting seasonal ice caps [*Kieffer et al.*, 2000; *Malin and Edgett*, 2001; *Kieffer*, 2003], and details regarding the stratigraphy and geomorphic evolution of the north polar layered materials [*Byrne and Murray*, 2002; *Edgett et al.*, 2003b; *Fishbaugh and Head*, 2005; *Milkovich and Head*, 2005].

2.5.1. Polar Geomorphology

[36] The best evidence for cyclic behavior of the Martian climate has for several decades been considered to be the layered materials found in both polar regions [e.g., *Murray et al.*, 1972; *Soderblom et al.*, 1973a]. Although attempts were made to correlate layers with variations in insolation resulting from long-term changes in Mars' orbital relations [e.g., *Blasius et al.*, 1982; *Cutts and Lewis*, 1982], MOC images revealed more and thinner layers, implying that the climate-related control of erosion and deposition must vary over timescales considerably less than the 10^5–10^6 year periods attributed to astronomical variations [*Malin and Edgett*, 2001]; some of these ideas have been explored recently in the context of high-resolution MOC results [*Laskar et al.*, 2002; *Milkovich and Head*, 2005]. MOC images also show important differences in layer outcrop expression between the north and south polar regions, and that the polar ice cap materials also erode differently [*Thomas et al.*, 2000].

[37] The south polar residual cap surface is smooth at decameter scale and has hectometer-scale depressions and mesas, fingerprint-patterned depressions, and evidence of subsurface subsidence and collapse, while the north polar cap exhibits a surface typically of closely spaced small buttes and shallow pits of only a few meters depth [*Thomas et al.*, 2000; *Malin and Edgett*, 2001]. Repeated monitoring of the south polar residual cap landforms confirmed that the materials are CO_2 because the scarps bounding the mesas

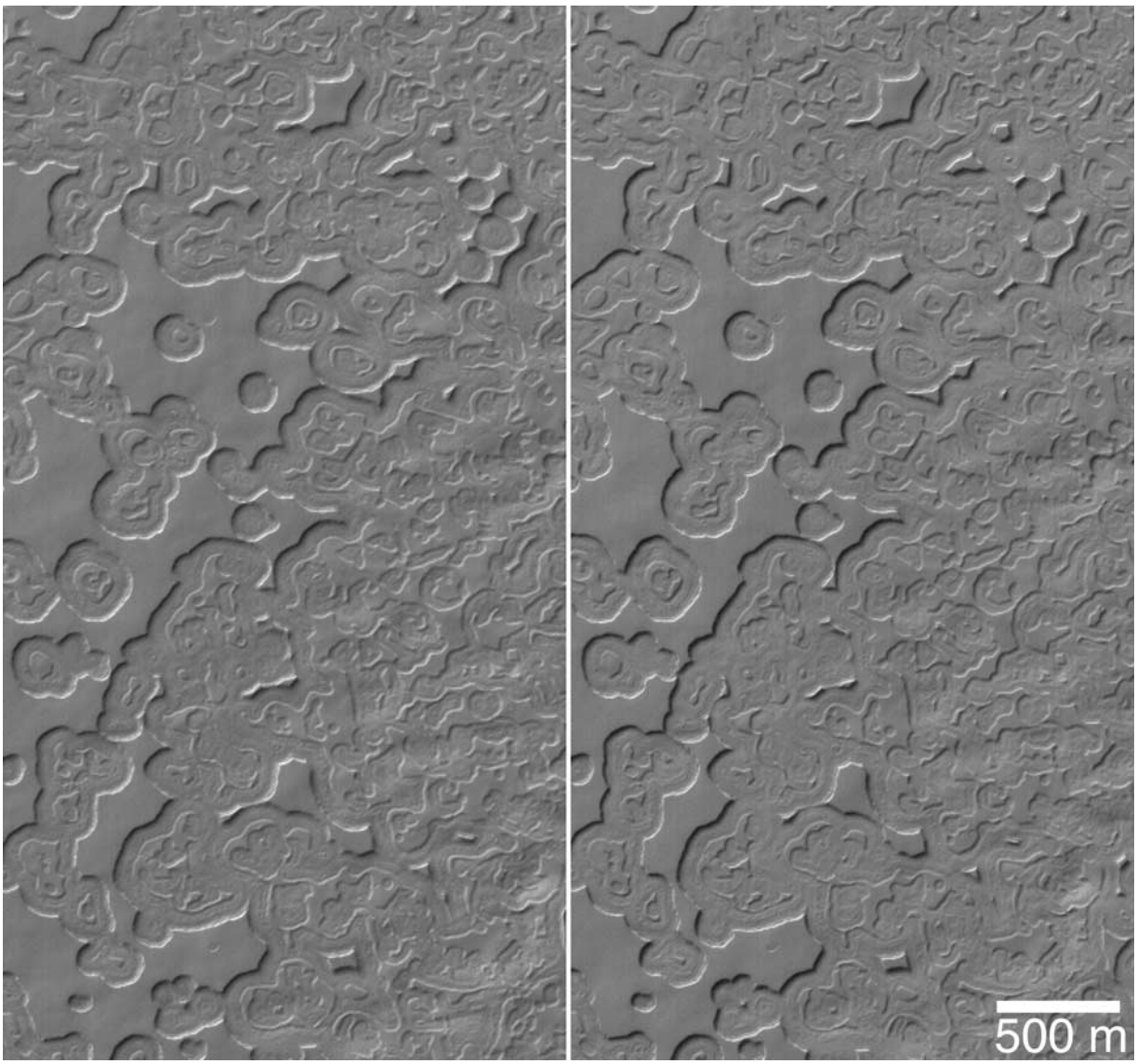

Figure 8. Two MOC images acquired at CTX resolution (6 m/pixel) ~1.1 Mars years apart, demonstrating that even at this scale, evidence of the ~3 m per Mars year scarp retreat can be seen (especially note the shrinkage of small buttes and mesas). The image on the left was acquired in 1999 and is a subframe of M04-01343; the image on the right is from 2001 and is a subframe of E07-01191. This area is located near 86.7°S, 346.3°W. Sunlight illuminates the scenes from the upper left.

and pits are retreating at a rate (~3 m/Mars year) that is measurable from orbit and too great for water ice [*Malin et al.*, 2001b]. The materials are composed of distinct units of several (~2 m) thick layers; the stratigraphy suggests that deposition, rather than the current erosion, may be the unusual event, and requires that Mars has had periods of colder climate within the past several centuries to millennia [*Malin et al.*, 2001b; *Thomas et al.*, 2005]. Monitoring the erosion (and possible depositional episodes?) over Martian years beyond that of the present MGS MOC coverage will help address the likely future lifetime and configuration of the south polar residual cap, and whether the current erosional regime is the norm.

[38] Although the south polar residual cap scarps retreat at rates of ~3 m per Mars year and CTX images have a resolution of 6 m/pixel, the MOC experience with images at resolutions poorer than 6 m/pixel (Figure 8) demonstrates that CTX images will have sufficient resolution to measure changes that have occurred on 1 Mars year intervals because, for example, a circular mesa with scarps retreating 3 m per Mars year will shrink by 6 m in diameter over that time interval. In addition, 6 m/pixel is certainly sufficient to measure changes occurring over >1 Mars year interval, and in some places on the south polar residual cap, the scarp retreat rate exceeds 3 m per Martian year [*Thomas et al.*, 2005]. An advantage of CTX over MOC for monitoring the south polar residual cap is its larger field of view. For the first time, the entire south polar CO_2 cap, including areas poleward of 87°S, which were not routinely observed by MOC because of the combined issues of the MOC narrow

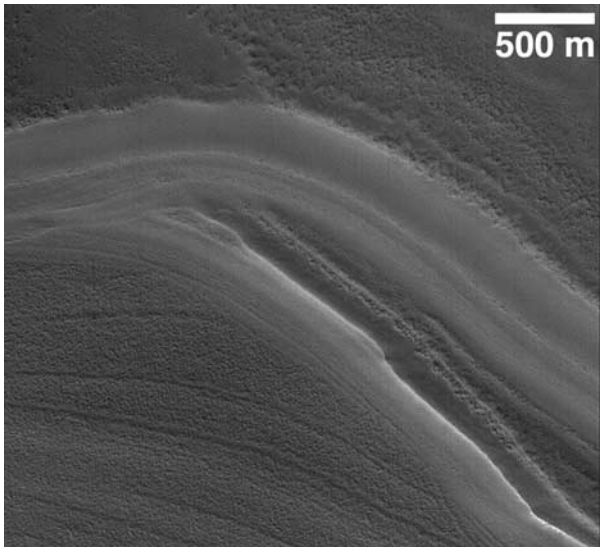

Figure 9. Examples of unconformable layers (two erosional unconformities) in the upper layered unit of the north polar layered terrain. This image covers an area 3 km wide and occurs near 80.7°N, 315.7°W. The figure is a subframe of MOC image S16-02196. Sunlight illuminates the scene from the lower left. At the time the image was acquired, the entire scene was covered with seasonal CO_2 frost.

field of view and the MGS orbital inclination, will be imaged at a spatial resolution sufficient to map and track the changes taking place.

2.5.2. Polar Stratigraphy

[39] MOC images show that polar layers exhibit bedding characteristics similar to sedimentary rock, including marker beds, lateral continuity over hundreds of kilometers, unconformities, vertical stratigraphic sequences with clearly defined formations or bedsets, and beds with differing degrees of resistance to erosion [*Malin and Edgett*, 2001; *Kolb and Tanaka*, 2001; *Byrne and Murray*, 2002; *Fishbaugh and Head*, 2005; *Tanaka*, 2005]. An example of an erosional unconformity identified in MOC images is shown in Figure 9. MOC images down to 1.5 m/pixel, in combination with MOLA topography, have opened the way to investigation of the polar layered deposit stratigraphy, and in the north polar region at least two [*Byrne and Murray*, 2002; *Edgett et al.*, 2003b; *Fishbaugh and Head*, 2005] but more likely three (Figure 10) distinct units have been identified. However, the narrow ground tracks of the MOC images have made connecting different outcrop sequences and the geometry of unconformities within the layers from one location to the next difficult to unambiguously identify and map. The spatial resolution, swath width, and ability to acquire stereopairs with MRO CTX will allow a much more complete investigation of the record and geometry of the polar layers, and thus provide a better understanding of the past depositional and erosional history of the polar regions.

2.5.3. Polar Seasonal Caps

[40] Dark spots and wind streaks have been known to form on dunes, sandy surfaces, and other terrain within the late winter and spring defrosting surfaces of the two seasonal polar caps since the earliest MOC and TES observations were obtained in 1997 and 1998 [*Edgett and Malin*, 2000; *Kieffer et al.*, 2000; *Malin and Edgett*, 2001]. The thermophysical properties of dunes and sand sheets might be a contributor to these phenomena. Some dark features that form within the seasonal south polar cap might be related to the formation of the low albedo/low temperature "cryptic terrain" of the seasonal south polar cap [*Kieffer et al.*, 2000; *Kieffer*, 2003]. Bright frost streaks have formed repeatedly at the same groups of craters since Viking observations [*Thomas et al.*, 1979]. Although MOC narrow-angle images were acquired that repeatedly monitored specific areas within the defrosting polar caps (e.g., "Inca City," Richardson dunes [*Malin and Edgett*, 2001]), CTX will provide a new opportunity, with its wider field of view, to observe and study the details of the repeatability of such features in the seasonal caps. CTX monitoring, in concert with higher-resolution MOC and HiRISE observations of these features, will help constrain their evolution. CTX will also be used in conjunction with MARCI to monitor larger seasonal frost features, such as the Mountains of Mitchel, which are especially sensitive to interannual changes [*Bonev et al.*, 2002].

2.6. Volcanic Features

[41] Volcanism played an important role in the evolution of the Martian surface [*Greeley and Spudis*, 1981], and volcanic materials have been found in some unexpected places, such as the floor of Gusev Crater [*McSween et al.*, 2004; *Martínez-Alonso et al.*, 2005]. Volcanism created constructs around central vents and formed plains lavas erupted from fissures; eruptions may also have created extensive tephra deposits [e.g., *Carr*, 1973; *Greeley and Spudis*, 1981; *Scott and Tanaka*, 1982; *Wilson and Head*, 1994]. Images from MOC and HRSC have led to examination of fine details in volcanic terrain [e.g., *Keszthelyi et al.*, 2000; *Mouginis-Mark*, 2002; *Neukum et al.*, 2004], while THEMIS infrared and visible images have revealed more small volcanoes and other features than were previously known from Mariner 9 and Viking coverage [*Mouginis-Mark and Christensen*, 2005]. CTX images will be acquired that further explore these landforms.

[42] Of particular interest in recent years, as noted earlier, has been the observation of an array of volcanic features in close contact with landforms interpreted to have involved flowing liquid water in the vicinity of and associated with the Cerberus Fossae, Athabasca Vallis, and Marte Valles systems. These surfaces display a pattern that is highly reminiscent of broken, rafted, and rotated plates, especially on the plains south of Cerberus and in Marte Valles. Some investigators have interpreted this pattern to indicate the material was emplaced as extremely fluid lava [*Keszthelyi et al.*, 2000; *Plescia*, 2003], while others have suggested the materials represent the remains of an ice-covered sea [*Murray et al.*, 2005], and the distinction between lava flows and mudflows is not in all cases obvious [*Malin and Edgett*, 2001]. Key evidence against the ice-covered sea model is the abundance of volcanic sources (vents) in the region [*Plescia*, 2003; *Sakimoto and Gregg*, 2004]. Also important is the observation that high-resolution MOC images show that small impact craters on these surfaces produced boulders (ice fragmentation tends to create smaller

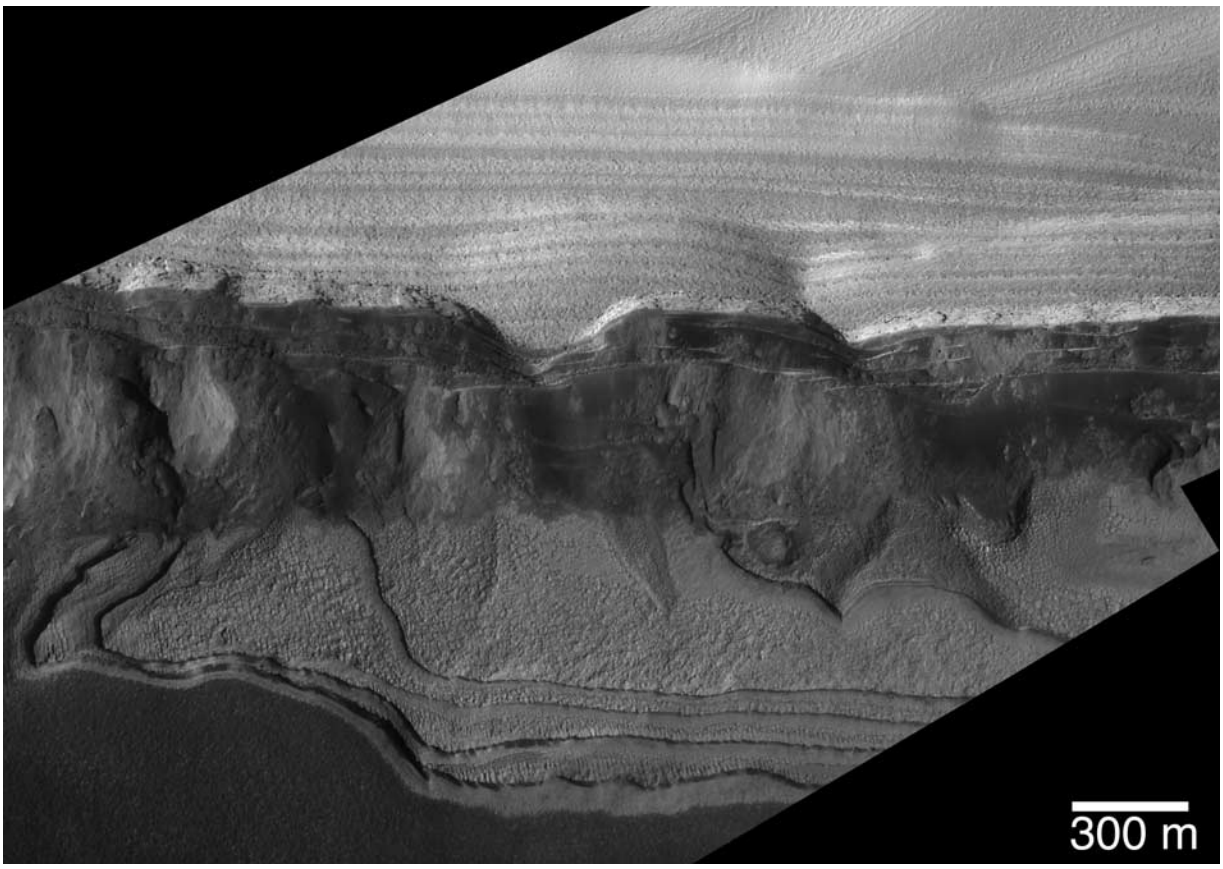

Figure 10. North polar layer stratigraphy exposed in the head scarp of Chasma Boreale. Three units, or bedsets, are visible. The uppermost unit has a light tone and distinct, nearly horizontal layers; the middle unit contains dark layers and thinner layers of more resistant, ledge-forming material; and the lower unit forms a broad shelf. The dark material in the middle unit is being shed and transported away from the site by wind to form dunes (not shown); the erosion of this sand-rich unit undermines the upper unit. This is a mosaic of two MOC images, S02-00486 and S02-01239. Sunlight illuminates the scene from the lower right; north is toward the left.

particles than boulders, and these would be expected to sublime away over very short timescales) and are not deformed or otherwise degraded in ways that experience with, for example, Europa, suggests should occur for impacts into an icy surface. Regardless of origin, the relative age of the flow materials is also strongly debated; a paucity of impact craters, and clear evidence that many of them are secondaries from a single impact in the region, suggests to some that the terrain is geologically quite young [*Hartmann and Berman*, 2000; *McEwen et al.*, 2005], while others point out that exhumation from beneath yardang-forming materials has also occurred, and may limit the utility of crater counts for determining the materials' age [*Malin and Edgett*, 2001]. Because of its 30 km field of view and MOC-like spatial resolution, CTX is ideal for further exploring the geomorphic relations among the variety of landforms in the Cerberus Fossae and Marte Valles regions. CTX data will help fill key gaps in existing MOC narrow-angle coverage, particularly along the courses of valleys and among flow features in these areas, and will complement existing, somewhat lower resolution views from HRSC.

[43] In addition to volcanic landforms, in recent years there has been renewed discussion of features associated with the larger Martian volcanoes that some have interpreted as glacial, and others as the products of mass movement. When first viewed in Mariner 9 and Viking orbiter images, lobate landforms located on terrain immediately west/northwest of the Olympus Mons basal scarp and the three Tharsis Montes were considered most likely to be landslide deposits [*Carr et al.*, 1977a]. The case for landslides was especially strong for the deposits at Olympus Mons, because of their association with the Olympus Mons basal scarp. The features off the west sides of the Tharsis Montes were more puzzling, leading some to suggest that they might have a glacial origin, especially because of the presence of semi-parallel ridges resembling (or so some considered) moraines [*Williams*, 1978; *Lucchitta*, 1981]. In addition to these ideas, of course, was the speculation that the basal scarp of Olympus Mons, itself, was an indication of a former, thicker ice sheet, i.e., the notion that Olympus Mons is a table mountain [*Hodges and Moore*, 1979]. Despite additional efforts based on Viking observations to characterize these materials as probable landslides [e.g.,

Zimbelman and Edgett, 1992], the glacial hypothesis has returned with the advent of Mars Express HRSC data. Modern proponents of this hypothesis have considered climate modeling [*Forget et al.*, 2006] as well as geomorphic expression [*Neukum et al.*, 2004; *Shean et al.*, 2005], and have added features on lower northwest flank of Hecates Tholus [*Hauber et al.*, 2005] to the list. Since 1999, many dozens of MOC narrow-angle images of these landforms have been acquired to address the geomorphology of these features, to help distinguish (by way of examining details not visible at the resolution of HRSC data) whether they are landslide or glacial deposits. MRO CTX imaging will help fill in the gaps in the MOC coverage and provide context for attendant HiRISE views of the materials, all in an effort to more uniquely determine which hypothesis is correct in each case.

2.7. Middle-Latitude Landforms

[44] Mariner 9 and Viking data revealed unusual surface textures within middle Martian latitudes (between roughly 30° and 60° latitude). *Soderblom et al.* [1973b] described a latitude-dependent mantle, *Squyres and Carr* [1986] noted in the cratered highlands and along midlatitude portions of the highland/lowland dichotomy boundary what they described as ''terrain softening,'' and there were observations of lineated valley floors in fretted terrain, aprons associated with massifs and mesas in the fretted terrain and in regions east of Hellas, and of ''concentric crater fill'' [*Sharp*, 1973; *Squyres*, 1979, 1989; *Zimbelman et al.*, 1989].

[45] The first high-resolution images received on Earth since the end of the Viking mission, from MGS MOC, revealed unexpected details. First, the regions known as ''softened terrain'' are (at meter to decameter scale) actually quite rough (''roughened terrain'' [*Malin and Edgett*, 2001]). Smooth-surfaced mantles in both hemispheres at middle latitudes are seen in MOC images to have become successively degraded into small, rugged hills and pits. *Mustard et al.* [2001] mapped occurrences of these materials, demonstrating their midlatitude association, and speculated that the degraded mantles might have once contained a volatile, such as water ice, that, upon sublimation and removal, created the roughened surfaces observed. In addition to these mantles, other midlatitude features have been identified in MOC and THEMIS VIS images that have been attributed to, or at least speculated to be related to, the presence or former presence of ice, including lobate flows on some midlatitude crater walls [*Baker*, 2003; *Milliken et al.*, 2003]; arcuate ridges at the base of slopes (often associated with gullies) and pitted crater floors [*Berman et al.*, 2005]; and ''pasted-on'' mantles, commonly on poleward-facing slopes [*Christensen*, 2003]. MOC and THEMIS images also provided further details regarding fretted terrain-type landforms such as the aprons that surround massifs west of Hellas and mesas north of Arabia [*Pierce and Crown*, 2003; *Crown et al.*, 2005] and the lineated valley floor materials [*Carr*, 2001; *Malin and Edgett*, 2001]. HRSC investigators explored additional midlatitude landforms, seen also in MOC and THEMIS data, that some investigators have attributed to midlatitude snow and glacial or glacier-like processes [*Head et al.*, 2005]. Taken together, these classes of midlatitude landforms have led to discussions of climate change and deposition of ice-rich mantles and snowpacks during previous obliquity excursions [e.g., *Head et al.*, 2003b].

[46] Some aspects of these midlatitude landforms have escaped general attention. For example, the lineated valley floor material in the fretted terrain north of Arabia Terra was long considered by some to indicate the flow or creep of ice-rich debris [e.g., *Squyres*, 1979, 1989]. However, MOC images revealed that the same lineated and pitted textures occur in materials on the floors of fretted terrain valleys that are closed at both ends, suggesting that down-valley flow (as would occur in glaciation) could not have occurred [*Malin and Edgett*, 2001]. Further, sometimes the terms various investigators used to label features limited the range of working hypotheses considered. The best example of this problem is that, when discussing the aprons that surround massifs east of Hellas and mesas north of Arabia, the aprons are invariably called ''debris aprons, '' implying a priori that they are composed of debris shed from the mesa or massif [*Squyres*, 1979, 1989; *Pierce and Crown*, 2003; *Mangold*, 2003]. The very act of naming the features, in this case, has limited consideration of alternatives, such as the possibility that the apron is actually composed of bedrock either as a layer or bedset that has different physical properties (perhaps, even, containing ice) or composition, and thus responding to erosion in a manner that differs from that of the material forming the bulk of the mesa or massif [*Malin and Eppler*, 1983], analogous to a pediment.

[47] The goal for CTX observations of midlatitude features is to test the hypotheses regarding flow of ice-rich materials by filling in the existing gaps in MOC narrow-angle camera coverage, acquiring 6 m/pixel stereo views, and providing context for key HiRISE images of these features. Owing to the large field of view, relative to MOC and HiRISE, entire fretted terrain valleys will be imaged at sufficient spatial resolution to examine the origin of lineated valley floor material through geomorphic analysis. Midlatitude crater floors and associated mantles and lobate wall features will be imaged, as well, because these same images will often include views of midlatitude gullies.

2.8. Impact Craters

[48] In planetary science, impact craters are ''tools of the trade.'' By comparing craters among planets and with model and experimental results, they probe subsurface stratigraphy and provide information about crustal properties, surface erosion processes, and various degrees of the timing of events that have shaped a surface. The proximity of Mars to the asteroid belt led a few investigators, prior to the Mariner 4 mission, to speculate that impact craters would occur on the planet [*Öpik*, 1950; *Tombaugh*, 1950]. The size and abundance of craters are strongly dependent on factors directly related to the Martian environment; small crater populations, for example, must reflect the complex interaction between primary influx, atmospheric filtering of incoming bodies, and surface processes modulated by climate. The smaller the crater, the shorter the timescale over which these interactions will have occurred. Over the past nine years, analysis of orbiter images, laser altimetry and initial Mars Express radar observations have made it clear that craters on Mars, at a range of scales from a few

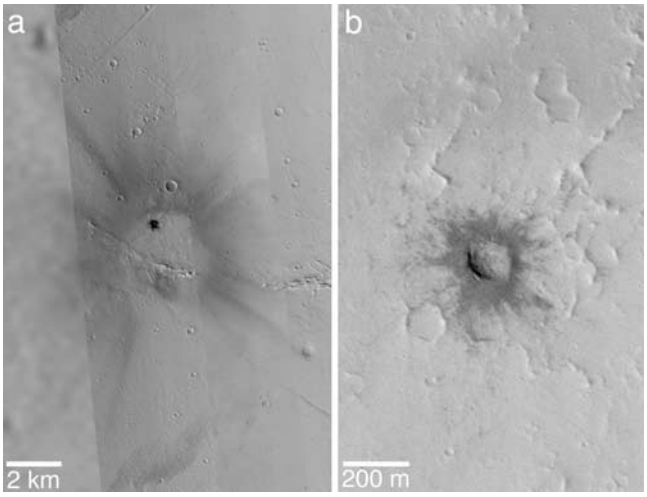

Figure 11. Young, fresh impact crater in Tharsis near 17.2°N, 113.8°W. The crater (right) is about 130 meters in diameter, but the impact blast affected dust on the surface for several kilometers distance from the crater. The distribution of the dark rays, an indicator of the surface dust disruption, is asymmetric, implying that the impactor came in from the south-southeast. While quite young, a dark feature (interpreted to be the crater plus its rays) was visible in Mariner 9 images from 1972 (e.g., DAS 7039378); thus the crater formed before that time. This is a composite of subframes of MOC images E05-01904, M21-00272, and M08-03697 and Viking image 516A55. North is up, and sunlight illuminates the MOC subframes from the lower left.

meters to >100 km, have been buried (and in some cases exhumed) and are an integral part of the planet's upper crust and stratigraphy [*Malin and Edgett*, 2001; *Frey et al.*, 2002; *Edgett and Malin*, 2004; *Picardi et al.*, 2005].

[49] On Mars, some craters exhibit "flow" or "rampart" ejecta (now termed "layered" according to a consortium of investigators [*Barlow et al.*, 2000]), believed by many to reflect the influence of subsurface volatiles on ejecta distribution [e.g., *Carr et al.*, 1977b; *Mouginis-Mark*, 1979; *Barlow and Perez*, 2003], and these have been used by some investigators to estimate where ancient ground ice or groundwater might once have occurred [e.g., *Kuzmin et al.*, 1989; *Costard*, 1989; *Barlow*, 2004]. In cases where subsurface water may have been present, an impact might set up conditions for a hydrothermal system that could last for some period of time [e.g., *Newsom*, 1980]. An unique, relatively fresh crater provisionally named Mojave, exhibits a plethora of distinct channels, alluvial fans, and debris flows, features that might indicate that the crater tapped a local source of volatiles, perhaps causing water from the subsurface to evaporate, condense and to rain down over the crater, or not. This particular crater remains a mystery [*R. M. E. Williams et al.*, 2004].

[50] With the advent of new data from MOC, THEMIS, and HRSC, plus MGS MOLA topography, there have been renewed investigations regarding the Martian cratering record and relation of craters to absolute age [*Hartmann et al.*, 1999; *Hartmann and Neukum*, 2001; *Neukum et al.*, 2004; *Hartmann*, 2005]. MOC images show some of the smallest, freshest craters on Mars, with dark ejecta and clear influence of the atmosphere on the redistribution of surface dust at the moment of impact (Figure 11), and THEMIS infrared images have shown very clearly which craters in the 2–10 km diameter range are the youngest on the planet [*Tornabene et al.*, 2005; *McEwen et al.*, 2005].

[51] CTX targeting efforts will include documentation, mosaics, and stereopair coverage of key impact craters on the Martian surface. Very young, pristine craters, such as those described by *Tornabene et al.* [2005] and the two larger impact craters near the summit of Olympus Mons will be investigated. One disadvantage of the 3-km-wide field of view of the MGS MOC was that it has been challenging to combine MOC and MOLA observations to get a clear picture of crater morphometry; CTX's ten times wider field of view will permit more complete mapping of craters at a scale not unlike that of MOC. CTX images will fill in the gaps in coverage in critical locations, such as the enigmatic Mojave Crater, and will provide context for HiRISE images designed to address the attributes of Martian craters.

2.9. Landing Sites and Exploration

2.9.1. Landing Site Imaging

[52] The MRO CTX investigation, both in its design and proposed implementation, has its roots in Sitefinder, a camera with 4 m/pixel resolution and a 20-km-wide field of view from 400 km altitude, proposed by Malin Space Science Systems in 1997 for the Mars Surveyor 2001 (Mars Odyssey) mission. Sitefinder was not selected for flight (indeed it was considered unresponsive to the Announcement of Opportunity). Its main objective was to scout future landing sites on Mars and assist mission planners in characterizing the entry, descent, and landing hazards (as well as rover trafficability) of any given candidate location. Today such capabilities are considered important to the Mars Exploration Program.

[53] High-resolution imaging is a key contributor to landing site certification. On MRO, the HiRISE instrument will provide the premier capability [*McEwen et al.*, 2007], with CTX acquiring contextual views. For small landing ellipses, such as the currently planned 20 km diameter circular "ellipse" for the Mars Science Laboratory (MSL) project, CTX can view an entire site with a single image, and obtain stereo with two. This will ensure a more rapid initial characterization of candidate sites, relative to the hundreds of 3-km-wide images obtained by the MGS MOC for the Mars Polar Lander, Mars Exploration Rovers, and Phoenix landing site selection efforts.

[54] In addition to their utility in selecting a landing site, MOC wide-angle and narrow-angle images were also used to document changes and monitor dust-raising events and cloud patterns over the sites, both before landings occurred and during landed missions. For example, MOC wide-angle images of Gusev Crater documented the dust storms that passed through the Spirit site in March 2005. These storms cleaned off dust from the rover solar panels, but they also altered the crater floor's albedo patterns such that they set up a stronger contrast between light and dark surfaces, which in turn may have contributed to the generation of the many dust devils observed by the rover in 2005 [*Cantor et al.*, 2006]. In addition to helping identify new landing

Table 1. Instrument Summary

Parameter	Value/Description
Resolution	6 meters/pixel from 300 km
Optics	f/3.25
Exposure time	1.3 msec/line minimum (1.88 msec/line nominal mapping)
Band pass	500–700 nm
Detector	Kodak KLI-5001G 5000-pixel linear array, 7 um pixels
Signal	12,000 e- at dark case (aphelion, i = 80, albedo 0.1) 153,000 e- at bright case (perihelion, i = 30, albedo 0.35)
Read noise	<100 e-
Worst-case SNR	40:1
Typical SNR	> 100:1
Digitization	12 bits/pixel linear, 300Ke- maximum single gain, no offset states dual DC-coupled amplifiers with settable black levels dual AD1672 3 MSPS ADCs, one per output channel
Power	~5 watts idle, ~7 watts imaging
Companding	12:8 bit companding
Scale	73 e-/DN
DRAM	256 MBytes (8 256 Mbit SDRAM chips)
SRAM	512Kx8 for companding tables
Digital control interface	Actel RT54SX32-S
Command	3-wire LVDS 515 Kbit/s
Data	3-wire LVDS 10 Mbit/s
Processor	none (all processing done in Spacecraft Flight Computer)

sites, CTX will be employed to monitor changes taking place at existing landing sites, particularly the dynamic Spirit site, and will track changes occurring at the short list of candidate sites for up-coming missions, such as Phoenix and MSL.

2.9.2. Exploration Imaging

[55] As of mid-2006, the MGS MOC narrow-angle camera has imaged about 5% of the Martian surface. These images have spatial resolutions ranging from 0.5 to ~15 m/pixel, with approximately 50% of MOC coverage at or worse than 6 m/pixel. The images are typically targeted one by one, by a Mars scientist, to ensure that quality science targets are selected. In this way, dozens of key sites, such as the Eberswalde delta and the alluvial fans in Mojave Crater, have become known. Many of the MOC narrow-angle images have also spawned new targets for MOC, and, we presume, for the MRO HiRISE. In other words, a feature of scientific interest seen in a MOC image of spatial resolution lower than ~2 m/pixel often leads to acquisition of an even higher resolution MOC image. In addition, it has been the observation of the MOC team that new and important results, sometimes very stunning results [e.g., *Malin et al.*, 2001a; *Malin and Edgett*, 2003], are discovered about once every 6–8 months. That pace of discovery has continued throughout the MGS extended mission, and it leads to the possibility that covering more than 5% of Mars will lead to new, important finds. Thus, in addition to the other science objectives described above, CTX will be targeted to acquire images in areas where the MGS MOC narrow-angle coverage is poor.

3. Instrument Description

[56] This section describes the MRO Context Camera (CTX) hardware, software, and operations. Table 1 summarizes the basic characteristics of the instrument. The CTX flight instrument, shown in Figure 12, was designed, fabricated, and is operated by Malin Space Science Systems.

3.1. History

[57] As noted in section 2.9.1, a CTX-like camera design was originally proposed for the Mars Surveyor 2001 Orbiter mission (later called Mars Odyssey), as Sitefinder. CTX mimics that design, using catadioptric optics similar to a scaled-up MARCI Medium Angle [*Malin et al.*, 2001a], and the same detector and basic system architecture. Sitefinder had about twice the spatial resolution, and a much smaller buffer compared to the CTX design (48 or 96 MB using 64 Mbit asynchronous DRAM versus 256 MB).

[58] The design was subsequently revisited as part of the 2003 Mars Science Orbiter (MSO) proposal effort (NASA eventually selected the Mars Exploration Rovers for that mission opportunity), where it was reconstituted as a color system with an internal processor, referred to as MARCI+. For MRO, the Science Definition Team recommended against flying a color system, and although the MRO Project briefly carried a desire for color, the absence of a firm requirement for color capability, and the desire to minimize cost and complexity while increasing reliability, led to a return to the panchromatic Sitefinder-like design.

3.2. Optics

[59] The CTX telescope is a 350 mm f/3.25 catadioptric with two front and two rear correcting elements (Figure 13). Its field of view is about 5.7 degrees, providing a ~30-km-wide swath from ~290 km altitude. Its mechanical structure is a composite configuration in which the structure that

Figure 12. The MRO Context Camera (CTX) telescope and electronics on a support bracket. Swiss Army knife for scale. A Schmidt-type catadioptric optical design, which uses lenses to focus light on a primary mirror, is used to achieve a large field of view. The telescope tube is made of graphite/cyanate-ester composite material.

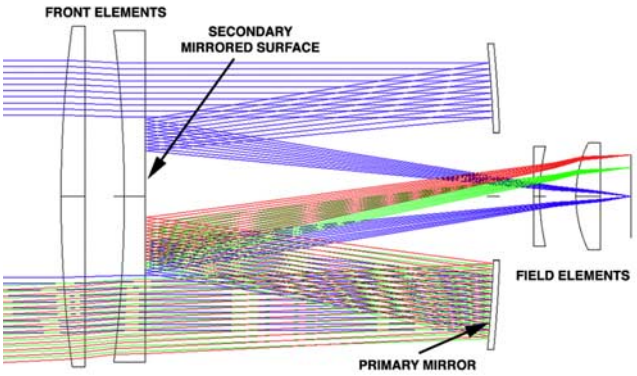

Figure 13. Ray traces, representing the optical path within the CTX telescope. The top portion of the diagram shows paths of on-axis rays (blue); the bottom portion shows paths of rays from the edge of the field of view (red) and midfield (green).

holds the optical elements to their precisely required locations (the metering structure) is graphite/cyanate-ester (GR/CE) (employed because of its very low coefficient of thermal expansion and high strength properties), and the elements are mounted in Invar and titanium cells. The primary mirror is hub-mounted on the same Invar cell that holds the rear correcting elements. The fast f/number both increases signal levels and hence SNR (signal-to-noise ratio), and also improves modulation transfer function (MTF) performance. The band pass is restricted to 500–700 nm to reduce atmospheric scatter at the blue end and reduce loss of detector MTF from diffusion at the red end (Figure 14). Scattered light levels from surfaces within the optics were minimized by darkened surfaces, baffling, and implementation of a grooved surface. Levels were less than 0.6% from a source 40° from the optic axis.

[60] A bakeout heater is wrapped around the optics metering structure to drive absorbed water out of the structure during cruise; the instrument is in optimal focus when the structure is completely dry. The heater also provides a mechanism for removing condensed volatiles from the optical surfaces by heating, should this be required.

3.3. Electronics

[61] The CTX electronics design is based on lessons learned from the MOC and MARCI instruments. Every effort has been made to simplify the design by reducing part count, while meeting the performance requirements of a high-resolution imaging system. Significant heritage from the MOC (gate array, clock drivers, DRAM/SRAM memory management) and MARCI (serial interface, analog design, power subsystem) designs led to a capable system with minimal design risk.

3.3.1. Detector

[62] The instrument is built around a Kodak KLI-5001G image sensor. This device is a 5000-element charge-coupled device (CCD) with 7 micron pixels, and an average quantum efficiency (QE) through the instrument band pass of >60%. It is fabricated in a N-type metal-oxide-semiconductor (NMOS) two-metal two-polysilicon process by Kodak Image Sensor Solutions in Rochester, New York. Correlated Double Sampling (CDS) is incorporated on-chip, in order to properly adjust for variations in base-level signals on a sample by sample basis. The device has dual readouts with a maximum readout rate of 12.5 MHz. Although the datasheet noise floor is fairly high (150 e- at room temperature and 12.5 MHz operation) performance is better at operating temperature and slower clocking; lab testing shows read noise as low as 100 e-.

[63] The good QE of the sensor, combined with the fast optics, provide signal-to-noise ratios (SNRs) in excess of 40:1 even at local solar times of 1700 hours, albedo of 0.1, minimum exposure time, and aphelion illumination. CTX can observe 8th magnitude stars with an exposure time of 45.9 milliseconds.

3.3.2. Analog Signal Processing

[64] Since CDS is provided on-chip on the CCD, the analog signal processing chain is considerably simplified from previous MSSS camera designs. The analog chain is duplicated for the two channels. Each chain consists of a current sink circuit, a unity-gain preamp, an amplifier with ~4X gain and DC offset, and a 12-bit analog-to-digital converter (ADC) with integral sample-and-hold. The preamp is located on the focal plane assembly (FPA) to preserve signal integrity over the flex cable to the electronics, and to minimize power dissipation near the detector. The National CLC432 dual opamp is baselined for the preamp and amplifier, and the Analog Devices AD1672 was selected for the ADC.

[65] Because we are not sampling the reset level independently, AC coupling of the signal followed by pixel-rate DC restoration is not feasible, nor do we want to give up the dynamic range that the digital-domain DC restoration used for MARCI would require. A traditional approach would be to use a line-rate clamp circuit to capture the dark reference pixel values, and using that reference, perform DC restoration on an AC-coupled signal. Unfortunately, this approach uses a fairly large number of components and is not power-efficient. Therefore we include a black-level DAC that allows a constant black level to be removed prior to amplification. The black level was established during calibration and can be changed via ground command, or via closed-loop control in the flight software if required.

[66] Because of the CCD's relatively high noise, we prefer to operate near its full well, when possible, to

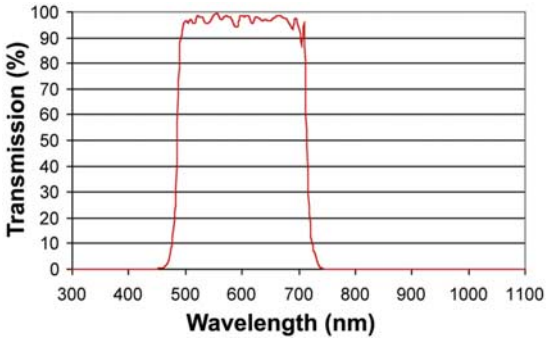

Figure 14. The CTX color filter band pass.

improve SNR. The digitization range is set to 300,000 electrons maximum, yielding a scale factor of about 73 electrons/DN, which matches the best expected noise performance of the CCD.

[67] The readout rate of the CCD is 2 MHz, leading to a pixel cycle time of 500 ns for an even-odd pixel pair. This is comfortably under the maximum sampling rate of 3 MHz for the AD1672.

3.3.3. Clock Generation

[68] The CCD requires 6 clock signals: a two-phase horizontal clock (H1/H2), a photosite-to-CCD transfer clock (T), a reset clock (R), and clamp and sample clocks (C and S) associated with the CDS. In addition, the dual ADCs require a single convert clock.

[69] The clocks are generated at logic levels in the digital electronics, and converted to the voltages required by the CCD using the Elantec clock drivers. Three devices are used: one with +5 V/−5 V rails driving the R and T clocks, one with +6.8 V/ground rails driving the H1/H2 clocks, and one with +15 V/ground rails driving the C and S clocks. The H1/H2 drivers are operated in parallel to supply extra drive for the high capacitive load of the H clocks.

[70] 3 V logic levels from the FPGA drive an ACT244 buffer with a VDD of 5 V. This is largely a holdover from an early design that employed discrete transistors to perform these tasks, as the Elantecs can be driven directly with 3 V logic, but we need the buffer to provide the 5 V ADC clock in any event.

3.3.4. Digital Electronics

[71] The digital electronics are responsible for clock generation, sampling of the CCD signal, conversion of the 12-bit samples to 8-bit encoded pixels, storage of the pixels, and finally readout of the pixels to the spacecraft.

[72] In a departure from the MARCI design, we have chosen to use a dedicated field-programmable gate array (FPGA) rather than a general-purpose processor to perform these functions. This decision was made to minimize cost and development complexity, and because the pixel rates required for this instrument are sufficiently high that an FPGA might be needed to perform some functions in any case. Rather than perform basic image capture in hardware and then process the data further within the instrument, we have chosen to transfer the raw data to the spacecraft flight computer (SFC) immediately, and do all additional processing there. Note that "SFC" is a collective term that refers to both the Command and Data Handler (C&DH) flight computer in which the CTX software resides, and the Solid-State Recorder, which provides bulk storage of science data. A disadvantage of relying in the SFC is the potential for resource conflict between image acquisition and processing and higher priority spacecraft functions, which would thereby limit CTX operations. Careful and integrated design of software between MSSS and Lockheed Martin greatly minimized this risk.

[73] The concept of providing only minimal data capture capability within the instrument was pioneered in the MOC design and continued in MARCI. Although its general-purpose processor normally supervises data acquisition in the MOC, a minimal mode of operation is provided by its gate arrays alone. By moving the processor's functionality to the SFC, considerable simplification to the design is realized.

3.3.4.1. Control Logic

[74] All control logic is implemented in a single Actel RT54SX32-S FPGA, with 32,000 usable gates and 227 user I/Os. The nominal clock rate for the FPGA is 20 MHz.

[75] The FPGA functions to be implemented were (1) 515 Kbps serial command interface from spacecraft, (2) 10 Mbps serial data interface to spacecraft, (3) DRAM interface, (4) ADC interface, (5) CCD clock generation, (6) 12-to-8 bit pixel compression/expansion (companding), and (7) commanding and DRAM readout. The design methodology was based on a state machine formulation of the needed functionality. Implementation was via synthesizable VHDL (VHSIC Hardware Design Language). The design used about 70% of the available logic resources of the FPGA.

3.3.4.2. DRAM Memory

[76] The instrument uses synchronous DRAMs for image storage. The CTX configuration uses eight devices of 32Mx8 organization, for a total capacity of 256 MB (268,435,456 bytes.) The DRAM is accessed linearly, one chip at a time, using a burst length of 4 with auto-precharge.

3.3.4.3. SRAM Memory

[77] A small SRAM is used to perform 12-to-8 bit companding in the FPGA. Each pixel DN value is used as an address into a 4096-byte table (one per channel) of 8-bit bytes. This effectively allows the conversion of 12-bit pixel data to 8-bit form without loss of information, by using square-root encoding (because the SNR scales as the square root of signal). Since the SRAM table can be changed in-flight, other forms of encoding (e.g., linear with offset) can be used as well.

[78] The UTMC UT8Q512 512Kx8 SRAM, with 25 ns cycle time, is used for the SRAM buffer. While much larger than required, this was the fastest 3.3 V SRAM available at the time.

3.3.4.4. Interface

[79] The spacecraft communicates with the instrument via a 3-signal (data, clock, and enable) synchronous serial interface, at a maximum clocking rate of 515 KHz. The interface clock clocks the command interface section of the FPGA and its outputs are synchronized to the system clock domain using dual flip-flops.

[80] The instrument communicates with the spacecraft's solid-state recorder via a 3-signal (data, clock, and enable) synchronous serial interface, at a maximum clocking rate of 10 MHz. The serial clock is divided down from the main system clock.

[81] Signal levels are converted to low voltage differential signal (LVDS) levels using UTMC LVDS driver and receiver chips.

3.3.5. Power Supply

[82] The instrument's digital electronics require +2.5 V for the FPGA core, +5 V for the ADCs, and +3.3 V for the gate array I/Os, SRAM, DRAM, and LVDS driver/receivers. The CCD clock rails are ground, +6.5, +5, +12, and −5 V. DC biases required by the CCD are +0.75, +3, +11, +15, and +5 V.

[83] The instrument requires 7 watts of power, most of it at +5 V or below. Interpoint 5 V and ±15 V converters are used to convert spacecraft +28 V power to ±15 V and +5 V. Power at 3.3 V and 2.5 V are provided by voltage regulators from the 5 V supply. The other low-current bias sources are

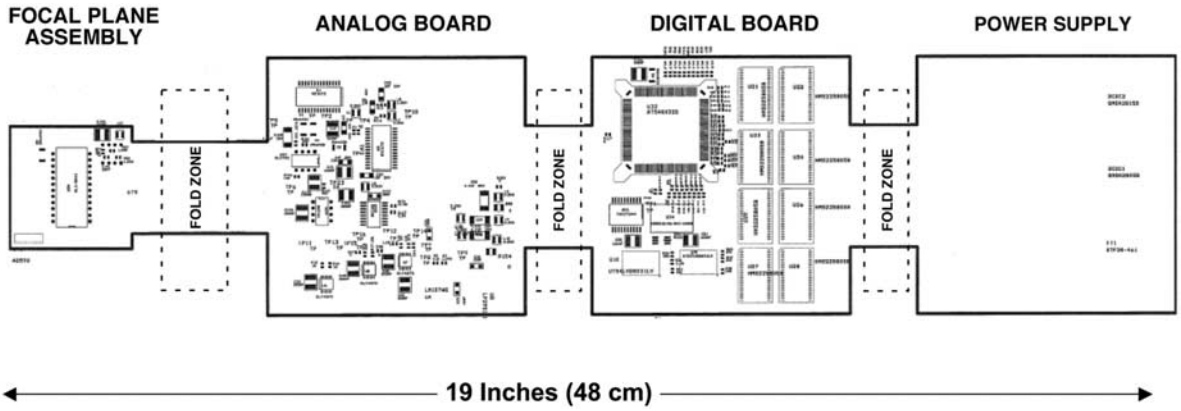

Figure 15. Configuration of CTX electronics during assembly. The rigid portion of rigid-flex system holds electronics parts; the flex portion allows the electronics to be folded one rigid portion over the other for packaging.

generated using regulators, opamps, resistor ladders, or zener diodes, as appropriate.

[84] An Interpoint electromagnetic interference (EMI) filter is used to reduce conducted emissions from the converters. Extensive passive filtering, including custom-wound baluns, are required to reduce noise on the converter outputs to acceptable levels.

3.3.6. Health Monitoring

[85] No internal instrument health monitoring is provided; such information would have required the added design and cost complication of internal sensors and software, and the simplicity of the design means there are very few instances that such internal information would assist problem mitigating efforts. Five temperature sensors (Analog Devices AD590) are provided, one on the focal plane, two on the electronics board, and two on the bakeout heater. These are monitored by the SFC.

3.4. Image Acquisition

[86] The instrument design has been optimized to take a single image, up to the size of the buffer, and transfer it to SFC memory via the serial interface. At 10 Mbit/s effective throughput, this process takes about 4 min. The spacecraft will travel 720 km (about 12° in latitude) in this time, precluding taking buffer-filling images in rapid sequence. However, an image occupying the entire buffer can cover 5 deg of latitude (300 km) in length, and, normally, the images will be much smaller, and hence take less time to read out. The trade between image length and the time interval between images will be made operationally.

[87] A very simple commanding interface is provided. Each command is a single 16-bit word in length; there are 16 possible commands, each with a 12-bit operand. The defined commands are: read 1MB DRAM block, set exposure time, set CCD start/count, set number of lines to acquire, set DAC reset level, set SRAM write pointer, write SRAM, set starting block for data acquisition, set mode, start image acquisition (“go”), and no operation.

3.5. Software

3.5.1. Flight Software

[88] As indicated above, there is no software resident in the instrument. All additional processing is performed in the SFC. This software has significant commonality with that developed by MSSS for the Mars Climate Orbiter MARCI [*Malin et al.*, 2001a] and Mars Odyssey THEMIS [*Christensen et al.*, 2004]. In fact, roughly 70% of the code, including commanding, data compression, power control, and buffer management, was inherited with few changes. Additionally, since for MRO the CTX data are transmitted to the solid-state recorder (SSR) rather than to C&DH DRAM, there is an additional processing step to retrieve data from the SSR; this was derived from the similar Mass Memory Card management used for THEMIS.

3.5.2. Ground Data System

[89] The Ground Data System has been developed directly from that built and utilized for nearly a decade for MGS MOC operations. As the instrument is quite similar to the MOC except for its field of view and resolution, the targeting, uplink generation, and data processing elements are virtually the same, requiring only the updating of a few instrument parameters. The resource allocation and conflict resolution software is also applicable, with most of the resources available for allocation moved from the instrument (as in the MOC) to the SFC (such as SFC DRAM space and processor cycles.) GDS changes to track SFC resources were incorporated as part of the MARCI GDS development effort.

3.6. Parts

3.6.1. Packaging

[90] As required by JPL, the parts packaging methodology uses mostly high-reliability ceramic components. Exceptions are the SDRAM and the Elantec clock drivers, which are only available as “plastic-encapsulated microcircuits” (PEMs). A qualification plan including acoustic imaging was used for these parts.

3.6.2. Board Layout

[91] Figure 15 illustrates the board layout. The system is packaged in an aluminum enclosure located beneath the optics. The analog, digital, and power electronics are contained on a rigid-flex nine-layer (power and ground planes and seven routing layers) two-sided board with three segments $4'' \times 4''$ in size. The board segments are sandwiched between housing sections for rigid edge support. Connectors carrying +28 V power, temperature sensors and data are hard-mounted to the boards.

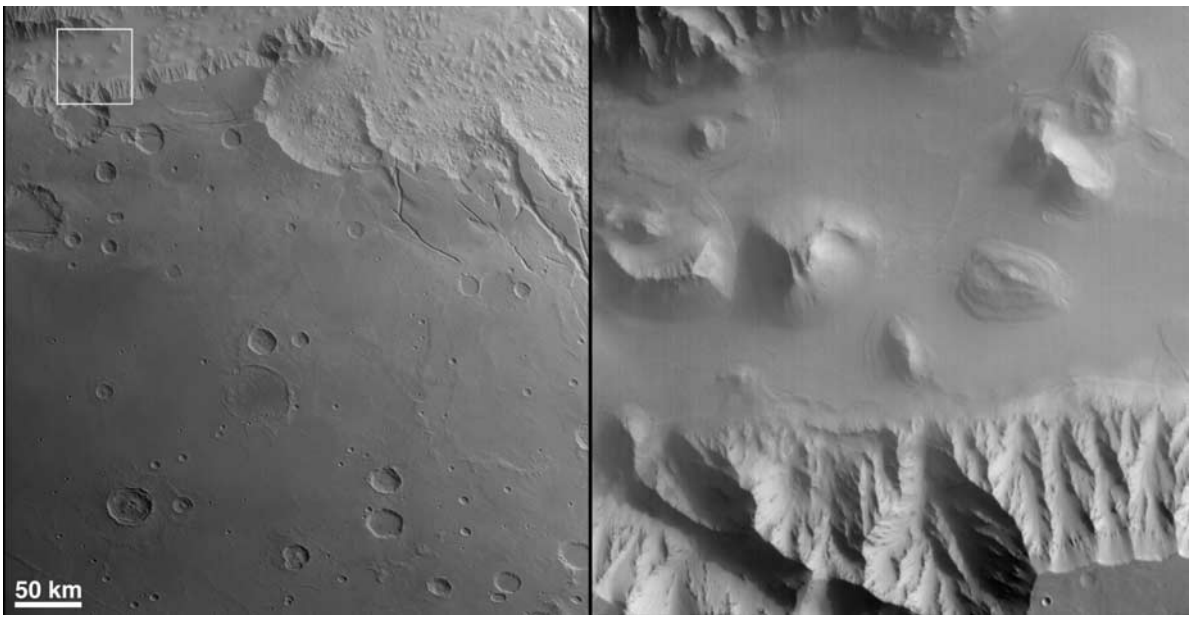

Figure 16. The first CTX image of Mars (left), showing an area south and east of the Valles Marineris. The image has a scale of about 87 meters (285 feet) per pixel, which is 14.5 times lower resolution than will be acquired when MRO is in its final mapping orbit. The enlargement (right) shows details in the white box. The image was acquired in the Martian morning, near 07:32 local time, with sunlight illuminating the scene from the upper right. The image (left) center is near 19°S, 51°W, and was acquired on 24 March 2006.

[92] The focal plane consists of a smaller section of the rigid-flex board holding the CCD package, passives, and preamps. The CCD is hard-mounted to the back of the optics, and the flex connects to the electronics board, removing the board and the electronics enclosure from the optical metering path.

3.7. Mission Operations

[93] CTX fulfills two roles on the MRO mission. During operations, the teams operating the other instruments will inform the CTX operations team at MSSS of the observations for which they need context images. The MRO project has a complex planning process that accommodates a wide range of priorities for such observations and whether they require interaction with the spacecraft or other instruments. Requests for contextual images are not considered interactive but occur on the same timescale as requests for interactivity.

[94] Following the MOC precedent, we define two types of basic observations: those that can be acquired at any time in the mission (time independent) and those that should be acquired on a specific orbit (time dependent). Time dependent observations tend to be ''targets of opportunity'' while time independent observations tend to be areas over which any observations will be acceptable. Time independent observations can carry time dependencies (e.g., take an image of this location at L_s between 100° and 110°), but these only become time dependent when a specific orbit is identified on which the observation can be made. We call the specific image acquisition meeting an observation requirement an ''event''. An observation can generate multiple events over the course of the mission. Observations can be defined geographically by a point, line or polygon, and can be defined temporally by L_s. The MRO Project calls our observation a ''region of interest'' and our event an observation.

[95] Software tools permit definition of observations as nadir and off-nadir. Off-nadir acquisitions are necessarily interactive, while nadir acquisitions are not. The MRO acquisition prioritization process defines ''must have'' acquisitions (interactive acquisitions that must be taken on either a specific orbit or specified multiple later orbits), ''coordinated'' acquisitions (where one instrument can request that other instruments also acquire data of the specified target) and ''ride-along'' acquisitions (wherein other instruments can choose to acquire data of the same target).

3.7.1. Data Return

[96] CTX has been allocated 12% of the total mission data return, which translates to $\geq$3 terabits of data. This data volume would cover about 9% of Mars at 6 m/pixel, but any overlap (for mosaics) or repeat coverage (for stereo or time series observations) reduces this percentage. An increase in the allocation by a small fraction is possible by transferring some of the MRO MARCI's data volume (7% of the mission total or just under 2 terabits) to CTX. But for all practical purposes, CTX coverage is still a limited resource.

3.8. Flight Operations

3.8.1. Cruise

[97] CTX acquired images of Earth and the Moon during a cruise phase instrument checkout on 8 September 2005. This checkout occurred at considerable distance from Earth

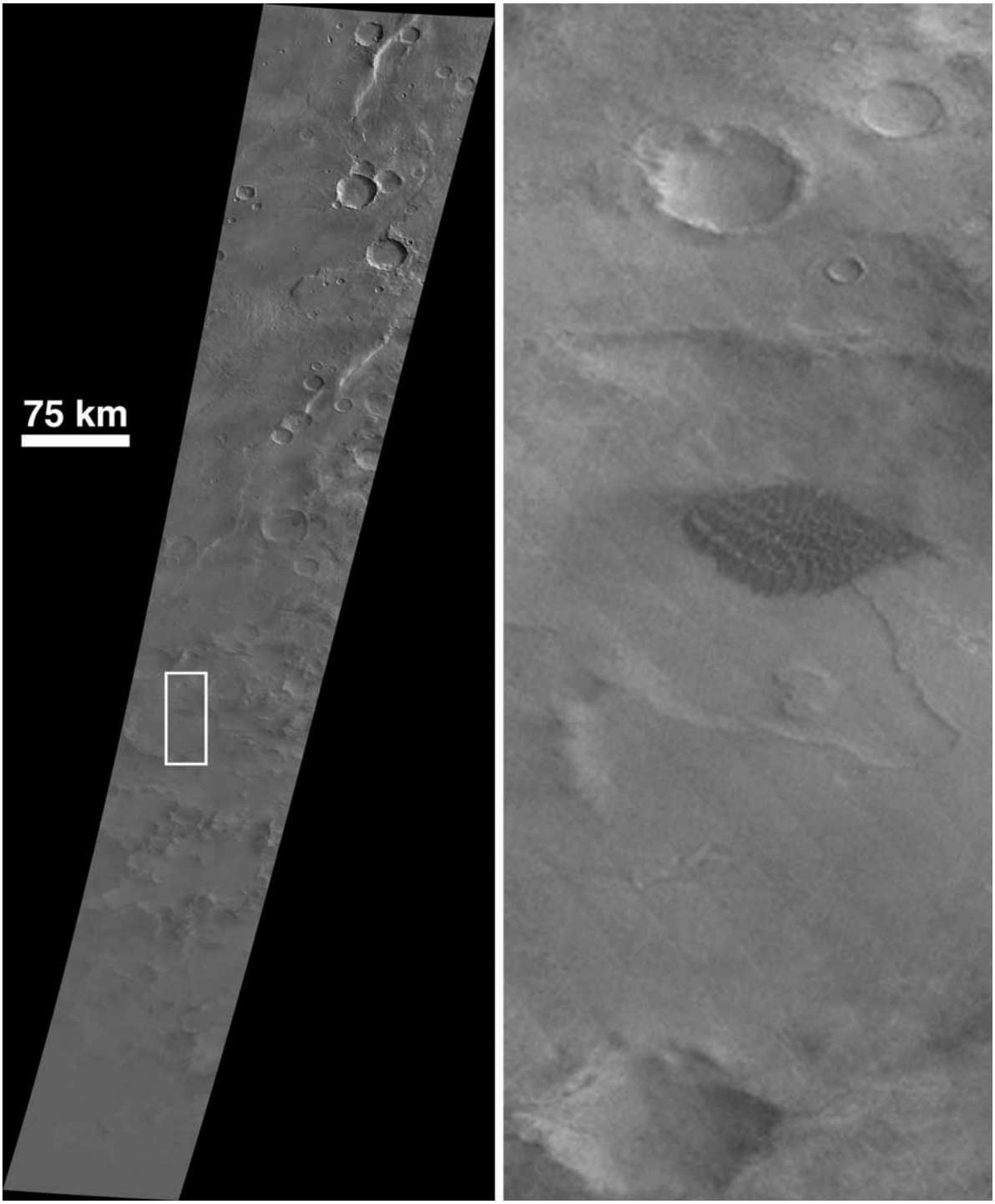

Figure 17. The second CTX image of Mars (left), covering 260 kilometers (~162 miles) at its widest point and about 122 kilometers (~76 miles) at its narrowest, some 1,590 kilometers (~988 miles) to the south. It covers an area of about 40,000 km^2 and is located west of the Argyre Basin. The change in width reflects the change in altitude of the MRO spacecraft as it descended toward periapsis over the south polar region. The white box outlines a portion of the image shown enlarged on the right. The illumination angle in this portion of the image (white box) was >85°, and the enlargement on the right displays brightness contouring (diagonal banding from upper left to lower right) resulting from the 12−8 bit companding (but also illustrates the excellent dynamic range of the system: compare this enlargement with the enlargement in the preceding illustration; both were taken at the same exposure setting). This image was acquired shortly after the first image, on the same orbit as that image (Figure 16), on 24 March 2006.

($\sim 10^7$ km) and the target bodies were very small relative to the field of view. These observations, along with images acquired of stars during cruise on 14 December 2005, provided important confirmation of the instrument's photometric and geometric calibration parameters.

3.8.2. Post-Mars Orbit Insertion

[98] After the 10 March 2006 orbit insertion, on the approach to the tenth orbit periapsis, the CTX, MARCI, and HiRISE, were turned on and the spacecraft pointed to nadir to permit image acquisition. This occurred on 24 March 2006. Although at an altitude >10 times farther from the planet than will occur during the nominal mission, the CTX data acquired show the image quality and illustrate the advantage of the 12-8 bit companding. Figures 16 and 17 show the two images that were obtained.

3.8.3. Post-Aerobraking

[99] CTX was powered off for the duration of the MRO aerobraking phase. We anticipate that the instrument will be turned on in late September/early October 2006 for a week or two of on-orbit calibration and instrument checkout activities before the 2006 Earth/Mars solar conjunction period. After conjunction, the Primary Science Phase of the MRO mission will begin.

[100] **Acknowledgments.** Malin Space Science Systems flight instruments are the product of a dedicated team effort; we thank the entire staff of MSSS for their roles in the design, fabrication, testing, calibration, and operation of the instrument. We also thank the MRO Project Scientist, Richard W. Zurek, and the MARCI/CTX Instrument Scientist, Amy Snyder Hale, both of the Jet Propulsion Laboratory (JPL), for their tireless contributions to this project. Reviews by Philip Christensen and especially Jeff Plescia are much appreciated. The CTX development effort was funded by NASA/JPL contract 1238365; the operations phase is funded by NASA/JPL contract 1275776.

References

Aharonson, O., M. T. Zuber, D. H. Rothaman, N. Schorghofer, and K. X. Whipple (2002), Drainage basins and channel incision on Mars, *Proc. Natl. Acad. Sci. U. S. A.*, *99*(4), 1780–1783, doi:10.1073/pnas.261704198.

Aharonson, O., N. Schorghofer, and M. F. Gerstell (2003), Slope streak formation and dust deposition rates on Mars, *J. Geophys. Res.*, *108*(E12), 5138, doi:10.1029/2003JE002123.

Ansan, V., and N. Mangold (2006), New observations of Warrego Valles, Mars: Evidence for precipitation and surface runoff, *Planet. Space Sci.*, *54*(3), 219–242, doi:10.1016/j.pss.2005.12.009.

Arvidson, R. E., F. Poulet, J.-P. Bibring, M. Wolff, A. Gendrin, R. V. Morris, J. J. Freeman, Y. Langevin, N. Mangold, and G. Bellucci (2005), Spectral reflectance and morphologic correlations in eastern Terra Meridiani, Mars, *Science*, *307*(5715), 1591–1594, doi:10.1126/science.1109509.

Baker, V. R. (2001), Water and the Martian landscape, *Nature*, *412*, 228–236, doi:10.1038/35084172.

Baker, V. R. (2003), Icy Martian mysteries, *Nature*, *426*, 779–780, doi:10.1038/426779.

Baker, V. R., and R. C. Kochel (1979), Martian channel morphology: Maja and Kasei Valles, *J. Geophys. Res.*, *84*, 7961–7983.

Baker, V. R., and D. J. Milton (1974), Erosion by catastrophic floods on Mars and Earth, *Icarus*, *23*(1), 27–41, doi:10.1016/0019-1035(74)90101-8.

Barlow, N. G. (2004), Martian subsurface volatile concentrations as a function of time: Clues from layered ejecta craters, *Geophys. Res. Lett.*, *31*, L05703, doi:10.1029/2003GL019075.

Barlow, N. G., and C. B. Perez (2003), Martian impact crater ejecta morphologies as indicators of the distribution of subsurface volatiles, *J. Geophys. Res.*, *108*(E8), 5085, doi:10.1029/2002JE002036.

Barlow, N. G., J. M. Boyce, F. M. Costard, R. A. Craddock, J. B. Garvin, S. E. H. Sakimoto, R. O. Kuzmin, D. J. Roddy, and L. A. Soderblom (2000), Standardizing the nomenclature of Martian impact crater ejecta morphologies, *J. Geophys. Res.*, *105*(E11), 26,733–26,738.

Bell, J. F., III, et al. (2004), Pancam multispectral imaging results from the Spirit rover at Gusev Crater, *Science*, *305*(5685), 800–806, doi:10.1126/science.110017.

Berman, D. C., and W. K. Hartmann (2002), Recent fluvial, volcanic, and tectonic activity on the Cerberus plains of Mars, *Icarus*, *159*, 1–17, doi:10.1006/icar.2002.6920.

Berman, D. C., W. K. Hartmann, D. A. Crown, and V. R. Baker (2005), The role of arcuate ridges and gullies in the degradation of craters in the Newton Basin region of Mars, *Icarus*, *178*, 465–486, doi:10.1016/j.icarus/2005.05.011.

Bibring, J.-P., et al. (2003), Perennial water ice identified in the south polar cap of Mars, *Nature*, *428*, 627–630, doi:10.1038/nature02461.

Blasius, K. R., J. A. Cutts, and A. D. Howard (1982), Topography and stratigraphy of Martian polar layered deposits, *Icarus*, *50*, 140–160, doi:10.1016/0019-1035(82)90122-1.

Bonev, B. P., P. B. James, J. E. Bjorkman, and M. J. Wolff (2002), Regression of the Mountains of Mitchel polar ice after the onset of a global dust storm on Mars, *Geophys. Res. Lett.*, *29*(21), 2017, doi:10.1029/2002GL015458.

Brackenridge, G. R., H. E. Newsom, and V. R. Baker (1985), Ancient hot springs on Mars: Origins and paleoenvironmental significance of small Martian valleys, *Geology*, *13*(12), 859–862, doi:10.1130/0091-7613(1985)13<859:AHSOMO>2.0.CO;2.

Burr, D. M., A. S. McEwen, and S. E. H. Sakimoto (2002a), Recent aqueous floods from the Cerberus Fossae, Mars, *Geophys. Res. Lett.*, *29*(1), 1013, doi:10.1029/2001GL013345.

Burr, D. M., J. A. Grier, A. S. McEwen, and L. P. Keszthelyi (2002b), Repeated aqueous flooding from the Cerberus Fossae: Evidence for very recently extant, deep groundwater on Mars, *Icarus*, *159*, 53–73, doi:10.1006/icar.2002.6921.

Burr, D. M., P. A. Carling, R. A. Beyer, and N. Lancaster (2004), Flood-formed dunes in Athabasca Valles, Mars: Morphology, modeling, and implications, *Icarus*, *171*, 68–83, doi:10.1016/j.icarus.2004.04.013.

Byrne, S., and B. C. Murray (2002), North polar stratigraphy and the paleoerg of Mars, *J. Geophys. Res.*, *107*(E6), 5044, doi:10.1029/2001JE001615.

Cantor, B. A. (2003), MGS-MOC observations of Martian dust storm activity, in *Sixth International Conference on Mars*, Abstract 3166, Lunar and Planet. Inst., Houston, Tex.

Cantor, B. A. (2007), MOC observations of the 2001 Mars planet-encircling dust storm, *Icarus*, *186*, 60–96, doi:10.1016/j.icarus.2006.08.019.

Cantor, B. A., P. B. James, M. Caplinger, and M. J. Wolff (2001), Martian dust storms: 1999 Mars Orbiter Camera observations, *J. Geophys. Res.*, *106*(E10), 23,653–23,688.

Cantor, B., M. Malin, and K. S. Edgett (2002), Multiyear Mars Orbiter Camera (MOC) observations of repeated Martian weather phenomena during the northern summer season, *J. Geophys. Res.*, *107*(E3), 5014, doi:10.1029/2001JE001588.

Cantor, B. A., K. M. Kanak, and K. S. Edgett (2006), Mars Orbiter Camera observations of Martian dust devils and their tracks (September 1997 to January 2006) and evaluation of theoretical vortex models, *J. Geophys. Res.*, *111*, E12002, doi:10.1029/2006JE002700.

Carr, M. H. (1973), Volcanism on Mars, *J. Geophys. Res.*, *78*, 4049–4062.

Carr, M. H. (1979), Formation of Martian flood features by release of water from confined aquifers, *J. Geophys. Res.*, *84*(B6), 2995–3007.

Carr, M. H. (2001), Mars Global Surveyor observations of Martian fretted terrain, *J. Geophys. Res.*, *106*(E10), 23,571–23,594.

Carr, M. H., and M. C. Malin (2000), Meter-scale characteristics of Martian channels and valleys, *Icarus*, *146*, 366–386, doi:10.1006/icar.2000.6428.

Carr, M. H., R. Greeley, K. R. Blasius, J. E. Guest, and J. B. Murray (1977a), Some Martian volcanic features as viewed from the Viking orbiters, *J. Geophys. Res.*, *82*(28), 3985–4015.

Carr, M. H., L. S. Crumpler, J. A. Cutts, R. Greeley, J. E. Guest, and H. Masursky (1977b), Martian impact craters and emplacement of ejecta by surface flow, *J. Geophys. Res.*, *82*(28), 4055–4065.

Chapman, M. G. (2002), Layered, massive, and thin sediments on Mars: Possible Late Noachian to Late Amazonian tephra?, in *Volcano-Ice Interactions on Earth and Mars*, edited by J. L. Smellie and M. G. Chapman, *Geol. Soc. Spec. Publ.*, *202*, 273–203.

Christensen, P. R. (1988), Global albedo variations on Mars: Implications for active aeolian transport, deposition, and erosion, *J. Geophys. Res.*, *93*(B7), 7611–7624.

Christensen, P. R. (2003), Formation of recent Martian gullies through melting of extensive water-rich snow deposits, *Nature*, *422*, 45–48, doi:10.1038/nature01436.

Christensen, P. R., et al. (2001), Mars Global Surveyor Thermal Emission Spectrometer experiment: Investigation description and surface science results, *J. Geophys. Res.*, *106*(E10), 23,823–23,872.

Christensen, P. R., et al. (2004), The Thermal Emission Imaging System (THEMIS) for the Mars 2001 Odyssey mission, *Space Sci. Rev.*, *110*, 85–130, doi:10.1023/B:SPAC.0000021008.16305.94.

Costard, F. (1989), The spatial distribution of volatiles in the Martian hydrolithosphere, *Earth Moon Planets*, *45*(3), 265–290, doi:10.1007/BF00057747.

Costard, F., F. Forget, N. Mangold, and J. P. Peulvast (2001), Formation of recent Martian debris flows by melting of near-surface ground ice at high obliquity, *Science*, *295*, 110–113, doi:10.1126/science.1066698.

Craddock, R. A., and A. D. Howard (2002), The case for rainfall on a warm, wet early Mars, *J. Geophys. Res.*, *107*(E11), 5111, doi:10.1029/2001JE001505.

Crown, D. A., L. F. Bleamaster III, and S. C. Mest (2005), Styles and timing of volatile-driven activity in the eastern Hellas region of Mars, *J. Geophys. Res.*, *110*, E12S22, doi:10.1029/2005JE002496.

Cushing, G. E., T. N. Titus, and P. R. Christensen (2005), THEMIS VIS and IR observations of a high-altitude Martian dust devil, *Geophys. Res. Lett.*, *32*, L23202, doi:10.1029/2005GL024478.

Cutts, J. A., and B. H. Lewis (1982), Models of climate cycles recorded in Martian polar layered deposits, *Icarus*, *50*, 216–244, doi:10.1016/0019-1035(82)90124-5.

Cutts, J. A., and R. S.U. Smith (1973), Eolian deposits and dunes on Mars, *J. Geophys. Res.*, *78*(20), 4139–4154.

Edgett, K. S. (2002), Low-albedo surfaces and eolian sediment: Mars Orbiter Camera views of western Arabia Terra craters and wind streaks, *J. Geophys. Res.*, *107*(E6), 5038, doi:10.1029/2001JE001587.

Edgett, K. S. (2005), The sedimentary rocks of Sinus Meridiani: Five key observations from data acquired by the Mars Global Surveyor and Mars Odyssey orbiters, *Mars*, *1*, 5–58, doi:10.1555/mars.2005.0002.

Edgett, K. S., and M. C. Malin (2000), New views of Mars eolian activity, materials, and surface properties: Three vignettes from the Mars Global Surveyor Mars Orbiter Camera, *J. Geophys. Res.*, *105*(E1), 1623–1650.

Edgett, K. S., and M. C. Malin (2004), The geologic record of early Mars: A layered, cratered, and ''valley-ed'' volume, *Lunar Planet. Sci.*, *XXXV*, Abstract 1188.

Edgett, K. S., M. C. Malin, R. M. E. Williams, and S. D. Davis (2003a), Polar- and middle-latitude Martian gullies: A view from MGS MOC after 2 Mars years in the mapping orbit, *Lunar Planet. Sci.*, *XXXIV*, Abstract 1038.

Edgett, K. S., R. M. E. Williams, M. C. Malin, B. A. Cantor, and P. C. Thomas (2003b), Mars landscape evolution: Influence of stratigraphy on geomorphology in the north polar region, *Geomorphology*, *52*(3–4), 289–297, doi:10.1016/S0169-555X(02)00262-3.

Eggleston, J. M., A. W. Patterson, J. E. Throop, W. H. Arant, and D. L. Spooner (1968), Lunar 'rolling stones,' *Photogramm. Eng.*, *34*, 246–255.

Ferri, F., P. H. Smith, M. Lemmon, and N. O. Rennó (2003), Dust devils as observed by Mars Pathfinder, *J. Geophys. Res.*, *108*(E12), 5133, doi:10.1029/2000JE001421.

Ferris, J. C., J. M. Dohm, V. R. Baker, and T. Maddock III (2002), Dark slope streaks on Mars: Are aqueous processes involved?, *Geophys. Res. Lett.*, *29*(10), 1490, doi:10.1029/2002GL014936.

Finkel, H. J. (1959), The barchans of southern Peru, *J. Geol.*, *67*, 614–647.

Fishbaugh, K. E., and J. W. Head III (2005), Origin and characteristics of the Mars north polar basal unit and implications for polar geologic history, *Icarus*, *174*, 444–474, doi:10.1016/j.icarus.2004.06.021.

Forget, F., R. M. Haberle, F. Montmessin, B. Levrard, and J. W. Head (2006), Formation of glaciers on Mars by atmospheric precipitation at high obliquity, *Science*, *311*, 368–371, doi:10.1126/science.1120335.

Frey, H. V., J. H. Roark, K. M. Shockey, E. L. Frey, and S. E. H. Sakimoto (2002), Ancient lowlands on Mars, *Geophys. Res. Lett.*, *29*(10), 1384, doi:10.1029/2001GL013832.

Geissler, P. E. (2005), Three decades of Martian surface changes, *J. Geophys. Res.*, *110*, E02001, doi:10.1029/2004JE002345.

Gendrin, A., et al. (2005), Sulfates in Martian layered terrains: The OMEGA/Mars Express view, *Science*, *307*(5715), 1587–1591, doi:10.1126/science.1109087.

Gilmore, M. S., and E. L. Phillips (2002), Role of aquicludes in formation of Martian gullies, *Geology*, *30*(12), 1107–1110, doi:10.1130/0091-7613(2002)030<1107:ROAIFO>2.0.CO;2.

Grant, J. A. (2000), Valley formation in Margaritifer Sinus, Mars, by precipitation-recharged ground-water sapping, *Geology*, *28*(3), 223–226, doi:10.1130/0091-7613(2000)28<223:VFIMSM>2.0.CO;2.

Greeley, R., and P. D. Spudis (1981), Volcanism on Mars, *Rev. Geophys.*, *19*(1), 13–41.

Greeley, R., J. D. Iversen, J. B. Pollack, N. Udovich, and B. White (1974), Wind tunnel simulations of light and dark streaks on Mars, *Science*, *183*, 847–849.

Greeley, R., A. Skypeck, and J. B. Pollack (1993), Martian aeolian features and deposits: Comparisons with general circulation model results, *J. Geophys. Res.*, *98*(E2), 3183–3196.

Greeley, R., et al. (2005), Martian variable features: New insight from the Mars Express Orbiter and the Mars Exploration Rover Spirit, *J. Geophys. Res.*, *110*, E06002, doi:10.1029/2005JE002403.

Greeley, R., et al. (2006), Gusev crater: Wind-related features and processes observed by the Mars Exploration Rover Spirit, *J. Geophys. Res.*, *111*, E02S09, doi:10.1029/2005JE002491.

Hartmann, W. K. (2005), Martian cratering 8: Isochron refinement and the chronology of Mars, *Icarus*, *174*, 294–320, doi:10.1016/j.icarus.2004.11.023.

Hartmann, W. K., and D. C. Berman (2000), Elysium Planitia lava flows: Crater count chronology and geological implications, *J. Geophys. Res.*, *105*(E6), 15,011–15,026.

Hartmann, W. K., and G. Neukum (2001), Cratering chronology and the evolution of Mars, *Space Sci. Rev.*, *96*, 165–194, doi:10.1023/A:1011945222010.

Hartmann, W. K., M. Malin, A. McEwen, M. Carr, L. Soderblom, P. Thomas, E. Danielson, P. James, and J. Veverka (1999), Evidence for recent volcanism on Mars from crater counts, *Nature*, *397*, 586–589, doi:10.1038/17545.

Hartmann, W. K., T. Thorsteinsson, and F. Sigurdson (2003), Martian hillside gullies and Icelandic analogs, *Icarus*, *162*, 259–277, doi:10.1016/S0019-1035(02)00065-9.

Hauber, E., et al. (2005), Discovery of a flank caldera and very young glacial activity at Hecates Tholus, Mars, *Nature*, *434*, 356–361, doi:10.1038/nature03423.

Head, J. W., L. Wilson, and K. L. Mitchell (2003a), Generation of recent massive water floods at Cerberus Fossae, Mars by dike emplacement, cryospheric cracking, and confined aquifer groundwater release, *Geophys. Res. Lett.*, *30*(11), 1577, doi:10.1029/2003GL017135.

Head, J. W., J. F. Mustard, M. A. Kreslavsky, R. E. Milliken, and D. R. Marchant (2003b), Recent ice ages on Mars, *Nature*, *426*, 797–802, doi:10.1038/nature02114.

Head, J. W., et al. (2005), Tropical to mid-latitude snow and ice accumulation, flow and glaciation on Mars, *Nature*, *434*, 346–351, doi:10.1038/nature03359.

Heldmann, J. L., and M. T. Mellon (2004), Observations of Martian gullies and constraints on potential formation mechanisms, *Icarus*, *168*, 285–304, doi:10.1016/j.icarus.2003.11.024.

Heldmann, J. L., O. B. Toon, W. H. Pollard, M. T. Mellon, J. Pitlick, C. P. McKay, and D. T. Andersen (2005), Formation of Martian gullies by the action of liquid water flowing under current Martian environmental conditions, *J. Geophys. Res.*, *110*, E05004, doi:10.1029/2004JE002261.

Hodges, C. A., and H. J. Moore (1979), The subglacial birth of Olympus Mons and its aureoles, *J. Geophys. Res.*, *84*(B14), 8061–8074.

Hoffman, N. (2002), Active polar gullies on Mars and the role of carbon dioxide, *Astrobiology*, *2*(3), 313–323.

Irwin, R. P., III, R. A. Craddock, and A. D. Howard (2005), Interior channels in Martian valley networks: Discharge and runoff production, *Geology*, *33*(6), 489–492, doi:10.1130/G21333.1.

Iversen, J. D., and B. R. White (1982), Saltation threshold on Earth, Mars, and Venus, *Sedimentology*, *29*(1), 111–119, doi:10.1111/j.1365-3091.1982.tb01713.x.

Jaumann, R., et al. (2005), Interior channels in Martian valleys: Constraints on fluvial erosion by measurements of the Mars Express High Resolution Stereo Camera, *Geophys. Res. Lett.*, *32*, L16203, doi:10.1029/2005GL023415.

Keszthelyi, L., A. S. McEwen, and T. Thordarson (2000), Terrestrial analogs and thermal models for Martian flood lavas, *J. Geophys. Res.*, *105*(E6), 15,027–15,050.

Kieffer, H. H. (2003), Behavior of solid CO_2 on Mars: A real zoo, in *Sixth International Conference on Mars*, Abstract 3158, Lunar and Planet. Inst., Houston, Tex.

Kieffer, H. H., T. N. Titus, K. F. Mullins, and P. R. Christensen (2000), Mars south polar spring and summer behavior observed by TES: Seasonal cap evolution controlled by frost grain size, *J. Geophys. Res.*, *105*(E4), 9653–9700.

Kolb, E. J., and K. L. Tanaka (2001), Geologic history of the polar regions of Mars based on Mars Global Surveyor data, *Icarus*, *154*(1), 22–39, doi:10.1006/icar.2001.6676.

Kuzmin, R. O., N. N. Bobina, E. V. Zabalueva, and V. P. Shashkina (1989), Structural inhomogeneities of the Martian cryolithosphere, *Sol. Syst. Res.*, *22*, 121–133.

Laskar, J., B. Levrard, and J. F. Mustard (2002), Orbital forcing of the Martian polar layered deposits, *Nature*, *419*, 375–377, doi:10.1038/nature01066.

Lee, P., C. S. Cockell, M. M. Marinova, C. P. McKay, and J. W. Rice Jr. (2001), Snow and ice melt flow features on Devon Island, Nunavut, Arctic Canada as possible analogs for recent slope flow features on Mars, *Lunar Planet. Sci.*, *XXXII*, Abstract 1809.

Lee, S. W., P. C. Thomas, and J. Veverka (1982), Wind streaks in Tharsis and Elysium: Implications for sediment transport by slope winds, *J. Geophys. Res.*, *87*(B12), 10,025–10,041.

Long, J. T., and R. P. Sharp (1964), Barchan-dune movement in Imperial Valley, California, *Geol. Soc. Am. Bull.*, *75*, 156–159.

Lowell, P. (1896), Markings in the Syrtis Major, *Pop. Astron.*, *4*(6), 289–296.

Lucchitta, B. K. (1978), A large landslide on Mars, *Geol. Soc. Am. Bull.*, *89*(11), 1601–1609, doi:10.1130/0016-7606(1978)89<1601:ALLOM>2.0.CO;2.

Lucchitta, B. K. (1981), Mars and Earth: Comparison of cold-climate features, *Icarus*, *45*(2), 264–303, doi:10.1016/0019-1035(81)90035-X.

Malin, M. C. (1976), Nature and origin of intercrater plains on Mars, in *Studies of Martian Geology*, Ph.D. dissertation, chap. 3, pp. 101–176, Calif. Inst. of Technol., Pasadena.

Malin, M. C., and M. H. Carr (1999), Groundwater formation of Martian valleys, *Nature*, *397*, 589–591, doi:10.1038/17551.

Malin, M. C., and K. S. Edgett (2000a), Sedimentary rocks of early Mars, *Science*, *290*, 1927–1937, doi:10.1126/science.290.5498.1927.

Malin, M. C., and K. S. Edgett (2000b), Evidence for recent groundwater seepage and surface runoff on Mars, *Science*, *288*, 2330–2335, doi:10.1126/science.288.5475.2330.

Malin, M. C., and K. S. Edgett (2001), Mars Global Surveyor Mars Orbiter Camera: Interplanetary cruise through primary mission, *J. Geophys. Res.*, *106*(E10), 23,429–23,570.

Malin, M. C., and K. S. Edgett (2003), Evidence for persistent flow and aqueous sedimentation on early Mars, *Science*, *302*, 1931–1934, doi:10.1126/science.1090544.

Malin, M. C., and K. S. Edgett (2005), MGS MOC: First views of Mars at sub-meter resolution from orbit, *Lunar Planet. Sci.*, *XXXVI*, Abstract 1172.

Malin, M. C., and D. B. Eppler (1983), Observations of Martian fretted terrain, in *Proceedings of the Fourth International Permafrost Conference in Fairbanks, Alaska*, pp. 787–791, Natl. Acad. Sci., Washington, D. C.

Malin, M. C., G. E. Danielson, A. P. Ingersoll, H. Masursky, J. Veverka, M. A. Ravine, and T. A. Soulanille (1992), Mars Observer Camera, *J. Geophys. Res.*, *97*(E5), 7699–7718.

Malin, M. C., J. F. Bell III, W. Calvin, R. T. Clancy, R. M. Haberle, P. B. James, S. W. Lee, P. C. Thomas, and M. A. Caplinger (2001a), The Mars Color Imager (MARCI) on the Mars Climate Orbiter, *J. Geophys. Res.*, *106*(E8), 17,651–17,672.

Malin, M. C., M. A. Caplinger, and S. D. Davis (2001b), Observational evidence for an active surface reservoir of solid carbon dioxide on Mars, *Science*, *294*, 2146–2148, doi:10.1126/science.1066416.

Mangold, N. (2003), Geomorphic analysis of lobate debris aprons on Mars at Mars Orbiter Camera scale: Evidence for ice sublimation initiated by fractures, *J. Geophys. Res.*, *108*(E4), 8021, doi:10.1029/2002JE001885.

Mangold, N., C. Quantin, V. Ansan, C. Delacourt, and P. Allemand (2004), Evidence for precipitation on Mars from dendritic valleys in the Valles Marineris area, *Science*, *305*(5680), 78–81, doi:10.1126/science.1097549.

Mars Channel Working Group (1983), Channels and valleys on Mars, *Geol. Soc. Am. Bull.*, *94*(9), 1035–1054, doi:10.1130/0016-7606(1983)94-<1035:CAVOM>2.0.CO;2.

Martin, L. J., and R. W. Zurek (1993), An analysis of the history of dust activity on Mars, *J. Geophys. Res.*, *98*(E2), 3221–3246.

Martínez-Alonso, S., B. M. Jakosky, M. T. Mellon, and N. E. Putzig (2005), A volcanic interpretation of Gusev Crater surface materials from thermophysical, spectral, and morphological evidence, *J. Geophys. Res.*, *110*, E01003, doi:10.1029/2004JE002327.

Maxwell, T. A., E. P. Otto, M. D. Picard, and R. C. Wilson (1973), Meteorite impact: A suggestion for the origin of some stream channels on Mars, *Geology*, *1*(1), 9–10, doi:10.1130/0091-7613(1973)1<9:MIASFT>2.0.CO;2.

McEwen, A. S. (1989), Mobility of large rock avalanches: Evidence from Valles Marineris, Mars, *Geology*, *17*(12), 111–1114, doi:10.1130/0091-7613(1989)017<1111:MOLRAE>2.3.CO;2.

McEwen, A. S., B. S. Preblich, E. P. Turtle, N. A. Artemieva, M. P. Golombek, M. Hurst, R. L. Kirk, D. M. Burr, and P. R. Christensen (2005), The rayed crater Zunil and interpretations of small impact craters on Mars, *Icarus*, *176*(2), 351–381, doi:10.1016/j.icarus.2005.02.009.

McEwen, A. S., et al. (2007), Mars Reconnaissance Orbiter's High Resolution Imaging Science Experiment (HiRISE), *J. Geophys. Res*, doi:10.1029/2005JE002605, in press.

McSween, H. Y., et al. (2004), Basaltic rocks analyzed by the Spirit rover in Gusev Crater, *Science*, *305*(5685), 842–845, doi:10.1126/science.3050842.

Mellon, M. T., and R. J. Phillips (2001), Recent gullies on Mars and the source of liquid water, *J. Geophys. Res.*, *106*(E10), 23,165–23,180.

Milkovich, S. M., and J. W. Head III (2005), North polar cap of Mars: Polar layered deposit characterization and identification of a fundamental climate signal, *J. Geophys. Res.*, *110*, E01005, doi:10.1029/2004JE002349.

Milliken, R. E., J. F. Mustard, and D. L. Goldsby (2003), Viscous flow features on the surface of Mars: Observations from high-resolution Mars Orbiter Camera (MOC) images, *J. Geophys. Res.*, *108*(E6), 5057, doi:10.1029/2002JE002005.

Milton, D. J. (1973), Water and processes of degradation in the Martian landscape, *J. Geophys. Res.*, *78*, 4037–4047.

Mouginis-Mark, P. J. (1979), Martian fluidized crater morphology: Variations with crater size, latitude, altitude, and target material, *J. Geophys. Res.*, *84*(B14), 8011–8022.

Mouginis-Mark, P. J. (1990), Recent water release in the Tharsis region of Mars, *Icarus*, *84*(2), 362–373, doi:10.1016/0019-1035(90)90044-A.

Mouginis-Mark, P. J. (2002), Prodigious ash deposits near the summit of Arsia Mons volcano, Mars, *Geophys. Res. Lett.*, *29*(16), 1768, doi:10.1029/2002GL015296.

Mouginis-Mark, P. J., and P. R. Christensen (2005), New observations of volcanic features on Mars from the THEMIS instrument, *J. Geophys. Res.*, *110*, E08007, doi:10.1029/2005JE002421.

Murchie, S., et al. (2007), Compact Reconnaissance Imaging Spectrometer for Mars on Mars Reconnaissance Orbiter, *J. Geophys. Res*, doi:10.1029/2006JE002682, in press.

Murray, B. C., L. A. Soderblom, J. A. Cutts, R. P. Sharp, D. J. Milton, and R. B. Leighton (1972), Geological framework of the south polar region of Mars, *Icarus*, *17*(2), 328–345, doi:10.1016/0019-1035(72)90004-8.

Murray, J. B., et al. (2005), Evidence from the Mars Express High Resolution Stereo Camera for a frozen sea close to Mars' equator, *Nature*, *434*, 352–356, doi:10.1038/nature03379.

Musselwhite, D. S., T. D. Swindle, and J. I. Lunine (2001), Liquid CO_2 breakout and the formation of recent small gullies on Mars, *Geophys. Res. Lett.*, *28*(7), 1283–1286.

Mustard, J. F., C. D. Cooper, and M. K. Rifkin (2001), Evidence for recent climate change on Mars from the identification of youthful near-surface ground ice, *Nature*, *412*, 411–414, doi:10.1038/35086515.

Neukum, G., et al. (2004), Recent and episodic volcanic and glacial activity on Mars revealed by the High Resolution Stereo Camera, *Nature*, *432*, 971–979, doi:10.1038/nature03231.

Newsom, H. E. (1980), Hydrothermal alteration of impact melt sheets with implications for Mars, *Icarus*, *44*(1), 207–216, doi:10.1016/0019-1035(80)90066-4.

Öpik, E. J. (1950), Mars and the asteroids, *Irish Astron. J.*, *1*(1), 22–24.

Picardi, G., et al. (2005), Radar soundings of the subsurface of Mars, *Science*, *310*, 1925–1928, doi:10.1126/science1122165.

Pierce, T. L., and D. A. Crown (2003), Morphologic and topographic analyses of debris aprons in the eastern Hellas region, Mars, *Icarus*, *163*, 46–65, doi:10.1016/S0019-1035(03)00046-0.

Pieri, D. C. (1976), Distribution of small channels on the Martian surface, *Icarus*, *27*(1), 25–50, doi:10.1016/0019-1035(76)90182-2.

Pieri, D. C. (1980), Martian valleys: Morphology, distribution, age, and origin, *Science*, *210*, 895–897.

Plescia, J. B. (2003), Cerberus Fossae, Elysium, Mars: A source for lava and water, *Icarus*, *164*, 79–95, doi:10.1016/S0019-1035(03)00139-8.

Pleskot, L. K., and E. D. Miner (1981), Time variability of Martian bolometric albedo, *Icarus*, *45*(1), 179–201, doi:10.1016/0019-1035(81)90013-0.

Poulet, F., P. J. -Bibring, J. F. Mustard, A. Gendrin, N. Mangold, Y. Langevin, R. E. Arvidson, B. Gondet, and C. Gomez (2005), Phyllosilicates on Mars and implications for early Martian climate, *Nature*, *438*, 627–632, doi:10.1038/nature04274.

Quantin, C., P. Allemand, N. Mangold, G. Dromart, and C. Delacourt (2005), Fluvial and lacustrine activity on layered deposits in Melas Chasma, Valles Marineris, Mars, *J. Geophys. Res.*, *110*, E12S19, doi:10.1029/2005JE002440.

Reiss, D., and R. Jaumann (2003), Recent debris flows on Mars: Seasonal observations of the Russell Crater dune field, *Geophys. Res. Lett.*, *30*(6), 1321, doi:10.1029/2002GL016704.

Reiss, D., S. van Gasselt, G. Neukum, and R. Jaumann (2004), Absolute dune ages and implications for the time of formation of gullies in Nirgal Vallis, Mars, *J. Geophys. Res.*, *109*, E06007, doi:10.1029/2004JE002251.

Sagan, C., and J. B. Pollack (1969), Windblown dust on Mars, *Nature*, *223*, 791–794.

Sagan, C., J. Veverka, P. Fox, R. Dubisch, J. Lederberg, E. Levinthal, L. Quam, R. Tucker, J. B. Pollack, and B. A. Smith (1972), Variable features on Mars: Preliminary Mariner 9 television results, *Icarus*, *17*(2), 346–372, doi:10.1016/0019-1035(72)90005-X.

Sagan, C., et al. (1973), Variable features on Mars, 2, Mariner 9 global results, *J. Geophys. Res.*, *78*(20), 4163–4196.

Sakimoto, S. E. H., and T. K. P. Gregg (2004), Cerberus Fossae and Elysium Planitia lavas, Mars: Source vents, flow rates, edifice styles and water interactions, *Lunar Planet. Sci.*, *XXXV*, Abstract 1851.

Schatz, V., H. Tsoar, K. S. Edgett, E. J. R. Parteli, and H. J. Herrmann (2006), Evidence for indurated sand dunes in the Martian north polar region, *J. Geophys. Res.*, *111*, E04006, doi:10.1029/2005JE002514.

Schorghofer, N., O. Aharonson, and S. Khatiwala (2002), Slope streaks on Mars: Correlations with surface properties and the potential role of water, *Geophys. Res. Lett.*, *29*(23), 2126, doi:10.1029/2002GL015889.

Scott, D. H., and K. L. Tanaka (1982), Ignimbrites of Amazonis Planitia region of Mars, *J. Geophys. Res.*, *87*(B2), 1179–1190.

Sharp, R. P. (1963), Wind ripples, *J. Geol*, *71*, 617–636.

Sharp, R. P. (1973), Mars: Fretted and chaotic terrains, *J. Geophys. Res.*, *78*(20), 4073–4083.
Sharp, R. P., and M. C. Malin (1975), Channels on Mars, *Geol. Soc. Am. Bull.*, *86*(5), 593–609, doi:10.1130/0016-7606(1975)86<593:COM>2.0.CO;2.
Shean, D. E., J. W. Head, and D. R. Marchant (2005), Origin and evolution of a cold-based tropical mountain glacier on Mars: The Pavonis Mons fan-shaped deposit, *J. Geophys. Res.*, *110*, E05001, doi:10.1029/2004JE002360.
Shinbrot, T., N.-H. Duong, L. Kwan, and M. M. Alvarez (2004), Dry granular flows can generate surface features resembling those seen in Martian gullies, *Proc. Natl. Acad. Sci. U. S. A.*, *101*(23), 8542–8546, doi:10.1073/pnas.0308251101.
Sinclair, P. C. (1969), General characteristics of dust devils, *J. Appl. Meteorol.*, *8*, 32–45.
Smith, P. H., et al. (1997), Results from the Mars Pathfinder camera, *Science*, *278*(5344), 1758–1765, doi:10.1126/science.278.5344.1758.
Soderblom, L. A., M. C. Malin, J. A. Cutts, and B. C. Murray (1973a), Mariner 9 observations of the surface of Mars in the north polar region, *J. Geophys. Res.*, *78*, 4197–4210.
Soderblom, L. A., T. J. Kriedler, and H. Masursky (1973b), Latitudinal distribution of a debris mantle on the Martian surface, *J. Geophys. Res.*, *78*, 4117–4122.
Soukhovitskaya, V., and M. Manga (2006), Martian landslides in Valles Marineris: Wet or dry?, *Icarus*, *180*(2), 348–352, doi:10.1016/j.icarus.2005.09.008.
Squyres, S. W. (1979), The distribution of lobate debris aprons and similar flows on Mars, *J. Geophys. Res.*, *84*(B14), 8087–8096.
Squyres, S. W. (1989), Urey Prize lecture: Water on Mars, *Icarus*, *79*(2), 229–288, doi:10.1016/0019-1035(89)90078-X.
Squyres, S. W., and M. H. Carr (1986), Geomorphic evidence for the distribution of ground ice on Mars, *Science*, *231*, 249–252.
Squyres, S. W., and A. H. Knoll (2005), Sedimentary rocks at Meridiani Planum: Origin, diagenesis, and implications for life on Mars, *Earth Planet. Sci. Lett.*, *240*, 1–10, doi:10.1016/j.epsl.2005.09.038.
Stewart, S. T., and F. Nimmo (2002), Surface runoff features on Mars: Testing the carbon dioxide formation hypothesis, *J. Geophys. Res.*, *107*(E9), 5069, doi:10.1029/2000JE001465.
Sullivan, R., P. Thomas, J. Veverka, M. Malin, and K. S. Edgett (2001), Mass movement slope streaks imaged by the Mars Orbiter Camera, *J. Geophys. Res.*, *106*(E10), 23,607–23,634.
Sullivan, R., et al. (2005), Aeolian processes at the Mars Exploration Rover Meridiani Planum landing site, *Nature*, *436*, 58–61, doi:10.1038/nature03641.
Supulver, K. D., K. S. Edgett, and M. C. Malin (2001), Seasonal changes in frost cover in the Martian south polar region: Mars Global Surveyor MOC and TES monitoring of the Richardson Crater dune field, *Lunar Planet. Sci.*, *XXXII*, Abstract 1966.
Tanaka, K. L. (2005), Geology and insolation-driven climatic history of Amazonian north polar materials on Mars, *Nature*, *437*, 991–994, doi:10.1038/nature04065.
Thomas, P., and P. J. Gierasch (1985), Dust devils on Mars, *Science*, *230*(4722), 175–177.
Thomas, P., and J. Veverka (1979), Seasonal and secular variation of wind streaks on Mars: An analysis of Mariner 9 and Viking data, *J. Geophys. Res.*, *84*(B14), 8131–8146.
Thomas, P., J. Veverka, and R. Campos-Marquetti (1979), Frost streaks in the south polar cap of Mars, *J. Geophys. Res.*, *84*(B9), 4621–4633.
Thomas, P. C., et al. (1999), Bright dunes on Mars, *Nature*, *397*, 592–594, doi:10.1038/17557.
Thomas, P. C., M. C. Malin, K. S. Edgett, M. H. Carr, W. K. Hartmann, A. P. Ingersoll, P. B. James, L. A. Soderblom, J. Veverka, and R. Sullivan (2000), North-south geological differences between the residual polar caps on Mars, *Nature*, *404*, 161–164, doi:10.1038/35004528.
Thomas, P. C., M. C. Malin, P. B. James, B. A. Cantor, R. M. E. Williams, and P. Gierasch (2005), South polar residual cap of Mars: Features, stratigraphy, and changes, *Icarus*, *174*, 5335–5359, doi:10.1016/j.icarus.2004.07.028.
Thorpe, T. E. (1982), Martian surface properties indicated by the opposition effect, *Icarus*, *49*(3), 398–415, doi:10.1016/0019-1035(82)90045-8.
Titus, T. N., H. H. Kieffer, and P. R. Christensen (2003), Exposed water ice discovered near the south pole of Mars, *Science*, *299*, 1048–1051, doi:10.1126/science.1080497.
Tombaugh, C. W. (1950), Geological interpretations of the markings on Mars, *Astron. J.*, *55*(6), 184, doi:10.1086/106434.
Tornabene, L. L., H. Y. McSween Jr., J. E. Moersch, J. L. Piatek, K. A. Milam, and P. R. Christensen (2005), Recognition of rayed craters on Mars in THEMIS thermal infrared imagery: Implications for Martian meteorite source regions, *Lunar Planet. Sci.*, *XXXVI*, Abstract 1970.
Treiman, A. H. (2003), Geologic settings of Martian gullies: Implications for their origins, *J. Geophys. Res.*, *108*(E4), 8031, doi:10.1029/2002JE001900.
Tsoar, H., R. Greeley, and A. R. Peterfreund (1979), Mars: The north polar sand sea and related wind patterns, *J. Geophys. Res.*, *84*(B14), 8167–8180.
Veverka, J., P. Thomas, and R. Greeley (1977), A study of variable features on Mars during the Viking primary mission, *J. Geophys. Res.*, *82*(28), 4167–4187.
Ward, A. W., K. B. Doyle, P. J. Helm, M. K. Weisman, and N. E. Witbeck (1985), Global map of eolian features on Mars, *J. Geophys. Res.*, *90*(B2), 2038–2056.
Wells, G. L., and J. R. Zimbelman (1989), Extraterrestrial arid surface processes, in *Arid Zone Geomorphology*, edited by D. S. G. Thomas, pp. 335–358, Halsted, New York.
Williams, D. A., R. Greeley, G. Neukum, E. Hauber, J. W. Head, and J. Murray (2004), Seeing Mars with new eyes: Latest results from the High Resolution Stereo Camera on Mars Express, *Geol. Soc. Am. Abstr. Programs*, *36*(5), 21.
Williams, R. M. E., and K. S. Edgett (2005), Valleys in the Martian rock record, *Lunar Planet. Sci.*, *XXXVI*, 1099.
Williams, R. M. E., and M. C. Malin (2004), Evidence for late stage fluvial activity in Kasei Valles, Mars, *J. Geophys. Res.*, *109*, E06001, doi:10.1029/2003JE002178.
Williams, R. M. E., K. S. Edgett, and M. C. Malin (2004), Young fans in equatorial crater in Xanthe Terra, Mars, *Lunar Planet. Sci.*, *XXXV*, Abstract 1415.
Williams, R. M. E., M. C. Malin, and K. S. Edgett (2005), Remnants of the courses of fine-scale, precipitation-fed runoff streams preserved in the Martian rock record, *Lunar Planet. Sci.*, *XXXVI*, 1173.
Williams, R. S., Jr. (1978), Geomorphic processes in Iceland and on Mars: A comparative appraisal from orbital images, *Geol. Soc. Am. Abstr. Programs*, *10*, 517.
Wilson, L., and J. W. Head III (1994), Mars: Review and analysis of volcanic eruption theory and relationships to observed landforms, *Rev. Geophys.*, *23*(3), 221–263.
Wilson, S. A., and J. R. Zimbelman (2004), Latitude-dependent nature and physical characteristics of transverse aeolian ridges on Mars, *J. Geophys. Res.*, *109*, E10003, doi:10.1029/2004JE002247.
Yizhaq, H. (2005), A mathematical model for aeolian megaripples on Mars, *Phys. A*, *357*, 57–63, doi:10.1016/j.physa.2005.05.070.
Zimbelman, J. R. (2000), Non-active dunes in the Acheron Fossae region of Mars between the Viking and Mars Global Surveyor eras, *Geophys. Res. Lett.*, *27*(7), 1069–1072.
Zimbelman, J. R., and K. S. Edgett (1992), The Tharsis Montes, Mars: Comparison of volcanic and modified landforms, *Proc. Lunar Planet. Sci. Conf.*, *22nd*, 31–44.
Zimbelman, J. R., S. M. Clifford, and S. H. Williams (1989), Concentric crater fill on Mars: An aeolian alternative to ice-rich mass wasting, *Proc. Lunar Planet. Sci. Conf.*, *19th*, 397–407.
Zurek, R. W., and L. J. Martin (1993), Interannual variability of planet-encircling dust storms on Mars, *J. Geophys. Res.*, *98*(E2), 3247–3259.

J. F. Bell III and P. C. Thomas, Department of Astronomy, Cornell University, 402 Space Sciences Building, Ithaca, NY 14853, USA.
W. M. Calvin, Department of Geological Sciences, University of Nevada, MS172, Reno, NV 89557, USA.
B. A. Cantor, M. A. Caplinger, K. S. Edgett, M. C. Malin, and M. A. Ravine, Malin Space Science Systems, P.O. Box 910148, San Diego, CA 92191-0148, USA.
R. T. Clancy, P. B. James, and M. J. Wolff, Space Science Institute, 4750 Walnut Street, Suite 205, Boulder, CO 80301, USA.
L. Edwards and R. M. Haberle, NASA Ames Research Center, Moffett Field, CA 94035, USA.
S. W. Lee, Denver Museum of Nature and Science, 2001 Colorado Boulevard, Denver, CO 80205, USA.